nature communications

Article

https://doi.org/10.1038/s41467-025-62569-1

Probiotic acoustic biosensors for noninvasive imaging of gut inflammation

Received: 28 March 2025

Accepted: 23 July 2025

Marjorie T. Buss[1], **Lian Zhu**[1], **Jamie H. Kwon**[2], **Jeffrey J. Tabor**[3,4,5,6] & **Mikhail G. Shapiro**[1,7,8] ✉

Inflammatory bowel diseases (IBD) affect millions of people globally, result in severe symptoms, and are difficult to diagnose and monitor – often necessitating the use of invasive and costly methods such as colonoscopies or endoscopies. Engineered gut bacteria offer a promising alternative due to their ability to persist in the gastrointestinal (GI) tract and sense and respond to specific environmental signals. However, probiotics that have previously been engineered to report on inflammatory and other disease biomarkers in the GI tract rely on fluorescent or bioluminescent reporters, whose signals cannot be resolved in situ due to the poor penetration of light in tissue, or on colorimetric reporters which rely on plating feces. To overcome this limitation, we introduce probiotic biosensors that can be imaged in situ using ultrasound – a widely available, inexpensive imaging modality providing sub-mm spatial resolution deep inside the body. These biosensors are based on the clinically approved probiotic bacterium *E. coli* Nissle, which we engineered to transiently colonize the GI tract, sense inflammatory biomarkers, and respond by expressing air-filled sound-scattering protein nanostructures called gas vesicles. After optimizing biomolecular signaling circuits to respond sensitively to the biomarkers thiosulfate and tetrathionate and produce strong and stable ultrasound contrast, we validated our living biosensors in vivo by noninvasively imaging antibiotic-induced inflammation in mice. By connecting cell-based diagnostic agents to ultrasound, these probiotic biosensors will potentially make it easier and cheaper to diagnose and monitor IBD or other GI conditions.

Inflammatory bowel diseases (IBD) affect millions of people[1,2], result in severe life-altering symptoms[3,4], and are caused by complex genetic and environmental factors leading to chronic intestinal inflammation[5,6]. Current methods to diagnose and monitor IBD, such as colonoscopies and biopsies, can be invasive, unpleasant, and costly[7], causing delays in diagnosis and treatment that can lead to complications and reduce the effectiveness of therapeutic interventions[8–14]. Other less invasive methods such as blood and stool tests often lack specificity due to inflammation elsewhere in the body and the short-lived nature of many disease-associated intestinal molecules. Moreover, they do not provide spatial information on the location of inflammation within the intestines, which can influence

---

[1]Division of Chemistry and Chemical Engineering, California Institute of Technology, Pasadena, CA, USA. [2]Division of Biology and Biological Engineering, California Institute of Technology, Pasadena, CA, USA. [3]Ph.D. Program in Systems, Synthetic, and Physical Biology, Rice University, Houston, TX, USA. [4]Department of Biosciences, Rice University, Houston, TX, USA. [5]Department of Bioengineering, Rice University, Houston, TX, USA. [6]Department of Chemical and Biomolecular Engineering, Rice University, Houston, TX, USA. [7]Andrew and Peggy Cherng Department of Medical Engineering, California Institute of Technology, Pasadena, CA, USA. [8]Howard Hughes Medical Institute, California Institute of Technology, Pasadena, CA, USA. ✉e-mail: mikhail@caltech.edu

treatment decisions[15–17]. A method to noninvasively visualize inflammatory biomarkers in situ in the gastrointestinal (GI) tract could greatly facilitate the monitoring, understanding, and diagnosis of IBD and other GI diseases[18–20].

Engineered probiotic bacteria could help diagnose IBD by colonizing the GI tract and sensing and reporting on specific signals in their environment[21–23]. Indeed, engineered bacteria have been developed to monitor intestinal biomarkers such as thiosulfate[24], tetrathionate[24,25], nitric oxide[26,27], calprotectin[28,29], and bleeding[30]. However, most of these probiotics report their findings through fluorescent or colorimetric reporters in the feces, which lack information about where in gut the inflammation takes place and require specialized laboratory equipment and protocols (e.g., flow cytometry) that may be difficult to translate to the clinic. Bioluminescent reporter strains[28,31] can be imaged in situ in mice, but have limited resolution due to light scattering and do not scale to larger animals or humans due to limited light penetration[32]. Bioluminescent bacteria have been coupled with a pill-based wireless electronic device[30], but this approach is complex, uses a large pill (~ 4.5 cm) that would not be easy for humans to swallow, and provides limited spatiotemporal information due to its rapid passage through the GI tract.

As an alternative readout, ultrasound readily propagates through tissue, allowing images to be acquired at several-centimeter depth with 100 micron-level spatial resolution[32]. Moreover, ultrasound imaging is inexpensive and ubiquitously available[33], increasing the translatability and potential impact of diagnostics that use ultrasound as a readout. Recently, it was demonstrated that bacteria can generate ultrasound contrast by expressing acoustic reporter genes (ARGs), which result in the production of air-filled protein nanostructures called gas vesicles that scatter sound waves[34,35]. However, ARG expression has not yet been incorporated into biosensors to detect specific molecular signals or used to visualize GI-colonizing bacteria.

Here we develop ARG-expressing probiotic cells as the basis for a “diagnostic yogurt” that could be ingested by a patient, transiently populate the GI tract, sense an inflammatory biomarker, and produce acoustic contrast that could be detected with a simple, noninvasive ultrasound scan the next day after probiotic administration (Fig. 1). To test this concept, we engineer the clinically approved probiotic *Escherichia coli* Nissle 1917 (EcN) to express ARGs in response to small molecule biomarkers of GI inflammation – focusing on thiosulfate and tetrathionate[24] – and develop protocols for their ultrasound detection in vivo after GI colonization. We optimize our acoustic biosensors through multiple rounds of genetic engineering so that they would produce detectable ultrasound contrast under physiologically relevant conditions (e.g., 37 °C, low biomarker concentrations). Finally, we validate mouse models of antibiotic-induced inflammation that exhibit elevated thiosulfate and noninvasively image inflammation in these mice using our optimized acoustic thiosulfate sensor.

Results

Engineered biosensing pathways enable the production of ultrasound contrast in response to inflammatory biomarkers

Thiosulfate ($S_2O_3^{2-}$) and tetrathionate ($S_4O_6^{2-}$) are biomarkers for intestinal inflammation arising from altered gut sulfur metabolism during colitis. Thiosulfate is generated when host cells detoxify hydrogen sulfide (H_2S)[36], whose production is thought to be upregulated during intestinal inflammation[37–40]. Reactive oxygen species present during inflammation further convert thiosulfate into the transient product tetrathionate[41]. Thiosulfate and tetrathionate have been shown to be elevated in DSS-induced[24] and *Salmonella*-induced[25] mouse models of colitis, respectively.

To develop living biosensors of thiosulfate and tetrathionate, we started with previously described fluorescent sensors of these molecules based on two-component systems (TCS) from *Shewanella*[24]. We aimed to replace the GFP in these constructs with ARGs to enable ultrasound imaging of the sensor bacteria in situ rather than detection of GFP in the feces via flow cytometry. We used a recently optimized ARG construct called bARG$_{Ser}$, derived from *Serratia sp*[35], placing it downstream of the promoter driven by *thsR* or *ttrR* response regulators, which are activated by thiosulfate or tetrathionate through *thsS* or *ttrS* sensor kinase receptors, respectively. We implemented these genetic pathways on a single medium-copy plasmid, with the TCS components constitutively expressed and with the Axe-Txe stability cassette[42] to form the plasmids thsSR-bARG$_{Ser}$ and ttrSR-bARG$_{Ser}$ (Fig. 2a).

Using these constructs, we observed ARG expression in *E. coli* in response to thiosulfate and tetrathionate one day after induction, but the initial ultrasound signal was lower than with an arabinose-inducible positive control construct pBAD-bARG$_{Ser}$ (Fig. S1). To

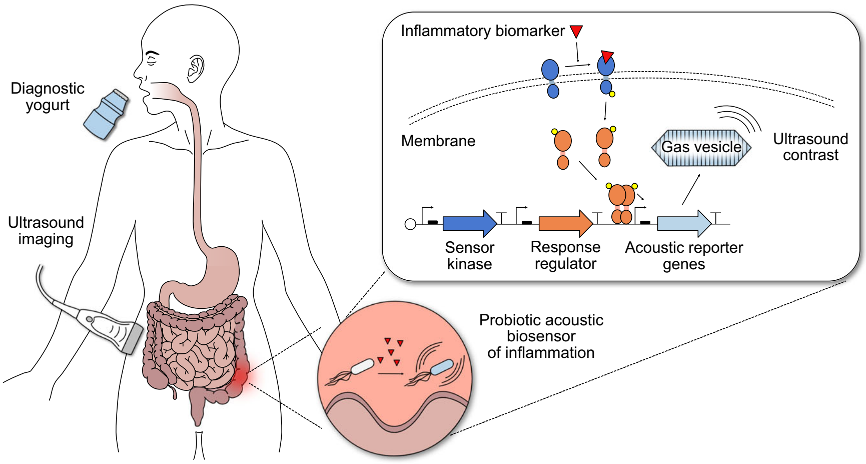

Fig. 1 | Concept of probiotic biosensors for ultrasound imaging of gastrointestinal (GI) inflammation. Patients consume yogurt containing diagnostic probiotic bacteria that transiently populate the GI tract. Using two-component systems (TCSs), these engineered bacteria sense inflammatory biomarkers, such as thiosulfate and tetrathionate, and express acoustic reporter genes (ARGs) that encode for gas vesicles (GVs) in response. Binding of the biomarker to the membrane sensor kinase protein triggers transcription of ARGs from a specific promoter via phosphorylation of a cytoplasmic response regulator protein; in the absence of the biomarker, phosphatase activity of the membrane sensor kinase keeps the system repressed. ARG-expressing bacteria can be detected via ultrasound imaging in patients, enabling ultrasound imaging of GI inflammation.

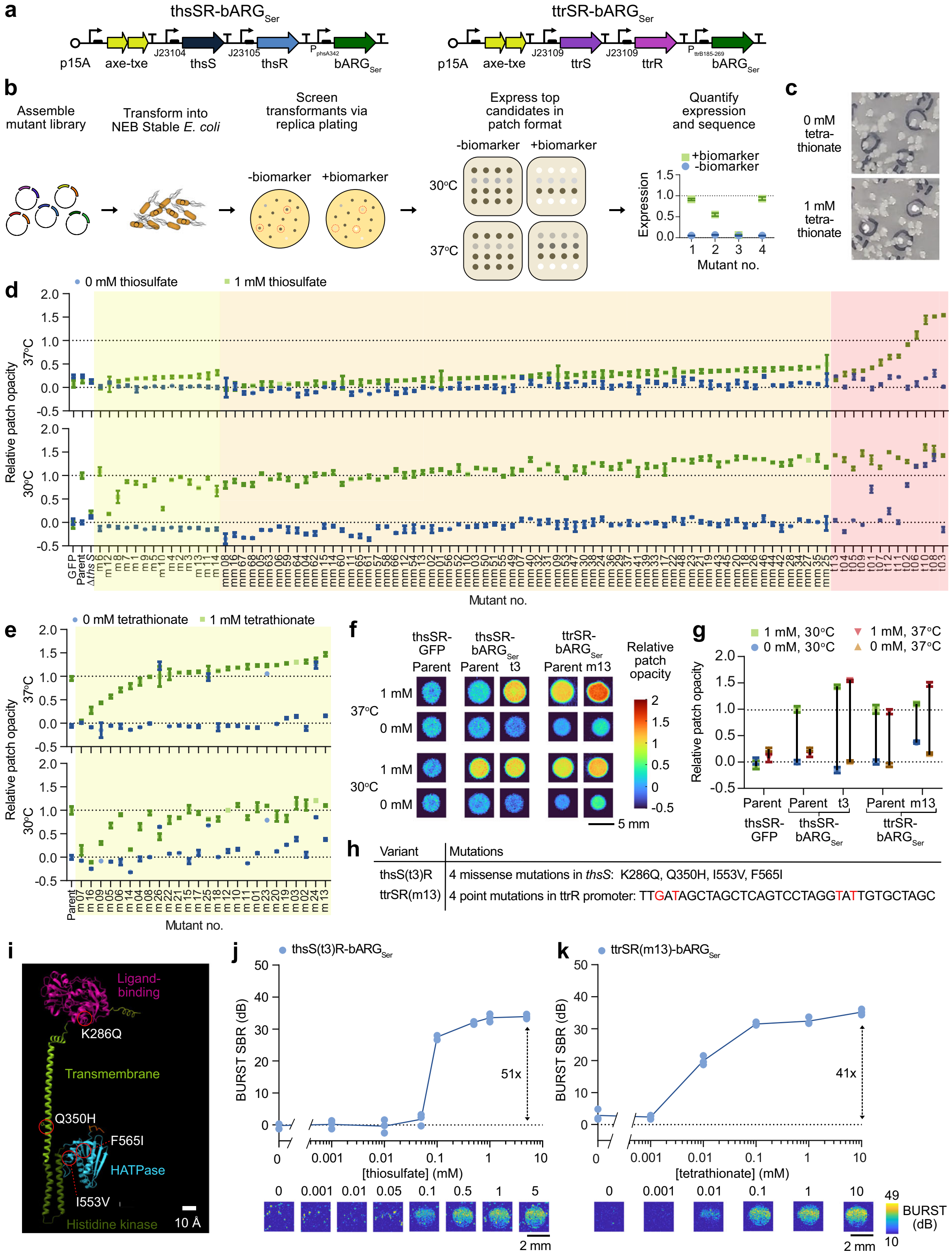

Variant	Mutations
thsS(t3)R	4 missense mutations in *thsS*: K286Q, Q350H, I553V, F565I
ttrSR(m13)	4 point mutations in ttrR promoter: TTGATAGCTAGCTCAGTCCTAGGTATTGTGCTAGC

improve performance, we engineered our genetic constructs using rapid mutagenesis and screening, relying on the optical opacity of gas vesicle-expressing bacterial colonies and replica-plating onto thiosulfate- or tetrathionate-containing media (Fig. 2b, c). In our screens, colonies that were visually more opaque with 1 mM thiosulfate/tetrathionate than without after one day of growth were picked and characterized in patch format at 30 °C and 37 °C. First, we tuned the expression levels of response regulators *thsR*/*ttrR* by mutagenizing their constitutive promoters using semi-random primers (Fig. S2a). This yielded several variants of thsSR-bARG$_{Ser}$ with slight improvements in opacity fold-change, but all variants still performed poorly at 37 °C compared to 30 °C (Fig. 2d). For ttrSR-bARG$_{Ser}$, this approach yielded several variants with a relative patch opacity of > 1 at 37 °C and 1 mM tetrathionate – in particular

Fig. 2 | Optimization of thiosulfate and tetrathionate sensors with ARGs as the output. **a** Plasmid diagrams of thiosulfate (thsSR-bARG$_{\text{Ser}}$) and tetrathionate (ttrSR-bARG$_{\text{Ser}}$) sensors with ARGs from *Serratia* sp. ATCC 39006 (bARG$_{\text{Ser}}$) as the output. **b** Protocol for screening for optimized variants of these sensors based on colony opacity. **c** Representative photographs of replica plates containing colonies at 0 and 1 mM tetrathionate. **d** Relative patch opacities from screening thsSR-bARG$_{\text{Ser}}$ variants mutated in the response regulator promoter (m01-m14, yellow shading), in both the response regulator and the sensor kinase promoters (mm01-mm68, orange shading), and in the sensor kinase gene *thsS* (t01-t13, red shading). **e** Relative patch opacities from screening ttrSR-bARG$_{\text{Ser}}$ variants mutated in the response regulator promoter (m01-m26, yellow shading). Representative images (**f**) and quantification in terms of relative opacity (**g**) of patches of the best-performing variants compared to the parent construct and a GFP control in NEB Stable *E. coli*. In **d**–**g**, a relative patch opacity of 0 corresponds to the parent construct at 0 mM and a relative patch opacity of 1 corresponds to the parent construct at 1 mM at 30 °C. Variants were ordered from lowest to highest relative patch opacity at 37 °C within each screening group. **h** Summary of mutations in the best-performing variants; see Table S1 for full sequences. **i** AlphaFold 3 ref. 111 structural prediction of *thsS(t3)* colored by predicted domains with the four mutations indicated by red circles; see Fig. S3 for more views of structural predictions. Representative BURST ultrasound images (bottom) and quantification of the signal-to-background ratio (SBR) (top) of the best variants for thsSR-bARG$_{\text{Ser}}$ (**j**) and ttrSR-bARG$_{\text{Ser}}$ (**k**) at varying thiosulfate/tetrathionate concentrations in *E. coli* Nissle (EcN) at 37 °C; cells were cast at 10^9 cells/mL in agarose. See Fig. S4 for corresponding xAM data. In **d**, **e**, and **g**, points represent the average of 2-4 biological replicates ($N = 2$ for points depicted in orange or yellow shading; $N = 4$ elsewhere) and error bars represent the standard deviation. In **j** and **k**, points represent biological replicates ($N = 3$, which were each averaged over 2 technical replicates) and solid lines connect the means.

the m13 variant (Fig. 2e). Similar trends were observed when mutating the GFP-expressing versions of the sensors (Fig. S2b–f).

Mutating the promoters driving both *thsR* and *thsS* simultaneously led to improved thiosulfate-sensing performance at 30 °C and 37 °C, but performance remained poor at 37 °C, leading us to hypothesize that the membrane sensor kinase *thsS* might not express well at the higher temperature. To address this issue, we mutated *thsS* using error-prone PCR and found several variants with increased opacity at 37 °C and 1 mM thiosulfate. In particular, the *thsS(t3)* variant exhibited a relative patch opacity of <0.25 at 0 mM and > 1 at 1 mM thiosulfate at both 37 °C and 30 °C (Fig. 2d). Overall, the thsS(t3)R-bARG$_{\text{Ser}}$ variant, which contained 4 missense mutations (K286Q, Q350H, I553V, and F565I) and 2 silent mutations in *thsS*, exhibited 10.5 times higher opacity at 37 °C and 1 mM thiosulfate than its parent construct (Fig. 2f–h, Fig. S3, Table S1). The mutated residues were distributed across the ligand-binding, transmembrane, and catalytic domains of the protein (Fig. 2i). The ttrSR(m13)-bARG$_{\text{Ser}}$ variant, which contained 4 point mutations in the *ttrR* constitutive promoter, had 1.5 times higher opacity at 37 °C and 1 mM tetrathionate than its parent (Fig. 2f–h, Table S1).

We characterized the ultrasound contrast produced by our two improved biosensors in EcN cultured at 37 °C with a range of thiosulfate and tetrathionate concentrations, observing increasing signal in response to increasing biomarker concentrations (Fig. 2j, k, Fig. S4). Using BURST imaging, a highly sensitive and specific ultrasound pulse sequence for gas vesicle detection[43], thsS(t3)R-bARG$_{\text{Ser}}$ and ttrSR(m13)-bARG$_{\text{Ser}}$ exhibited maximal fold-changes of 51 and 41, respectively, in response to their cognate analytes. This switching performance is high compared to many inducible biosensors in the literature[24,27,28,44]. Similar trends were observed under xAM imaging, a complementary, non-destructive ultrasound imaging mode also popular for gas vesicle detection[45] (Fig. S4).

Recombinase-based switching increases sensor signal in response to biomarkers

To increase ultrasound signal and biomarker sensitivity even further, we incorporated a recombinase into our optimized two-component sensors. We placed the serine integrase Bxb1 downstream of our *thsR*-activated promoter, and placed bARG$_{\text{Ser}}$ downstream of the strong constitutive promoter P7[46], which we flanked with Bxb1 recognition sequences *attB* and *attP*. We included a temperature-responsive terminator upstream of Bxb1 to reduce leaky expression outside the body below 37 °C[47] (Fig. 3a). Before cells are exposed to thiosulfate, the P7 promoter points towards two strong terminators and bARG$_{\text{Ser}}$ is not expressed. When cells are exposed to thiosulfate, the thsS(t3)R pathway triggers Bxb1 expression, which catalyzes irreversible site-specific recombination between *attB* and *attP*, flipping the direction of P7 and resulting in constitutive bARG$_{\text{Ser}}$ expression. We named this construct thsS(t3)R-Bxb1_P7-bARG$_{\text{Ser}}$.

We compared thsS(t3)R-Bxb1_P7-bARG$_{\text{Ser}}$ and thsS(t3)R-bARG$_{\text{Ser}}$ in EcN at 37 °C, measuring the BURST and xAM ultrasound signals after exposing the cells to a range of thiosulfate concentrations (Fig. 3b, c, Fig. S5a, Fig. S6a, b). The recombinase-based biosensor produced 2.5-fold higher ultrasound signal in 100 μM thiosulfate compared to the non-recombinase construct and exhibited a maximal fold-change of 100. The recombinase-based circuit also showed higher thiosulfate sensitivity, shifting the half-maximum Hill equation constant for BURST signal from 76.4 to 48.2 μM (Table S2).

We also implemented the Bxb1 switching approach in the fluorescent protein version of the thiosulfate sensor, forming plasmid thsS(t3)R-Bxb1_P7-GFP_mCherry (Fig. 3d). Flow cytometry of thsS(t3)R-Bxb1_P7-GFP_mCherry versus thsS(t3)R-GFP_mCherry EcN after inducing with a range of thiosulfate concentrations at 37 °C demonstrated increased GFP fluorescence in response to thiosulfate (19.2-fold higher at 100 μM thiosulfate), increased sensitivity (the Hill constant decreased from 105 to 57.2 μM), and distinct negative and positive ("unflipped" and "flipped") GFP populations with addition of the Bxb1 switch (Fig. 3e, f, Fig. S5b, Table S2).

We obtained similar results when implementing the Bxb1 switch in the ARG and fluorescent versions of our tetrathionate sensor (Fig. S5c, d, Fig. S6c–j, Table S2). These results demonstrate that addition of a Bxb1 switch with the strong constitutive promoter P7 improves the performance of two-component system EcN biosensors with both acoustic and fluorescent outputs.

Probiotic biosensors colonize the GI tract and respond to their cognate biomarkers

To prepare for disease biosensing in vivo, we first aimed to demonstrate that EcN-based probiotic agents could colonize the GI tract and produce ultrasound contrast in response to externally supplied small molecules. To reduce colonization resistance by native fauna, we treated the mice with streptomycin starting two days prior to probiotic administration[48–51] and continuing through the course of the experiment, and we used EcN with a spontaneous mutation in the *rpsL* gene conferring streptomycin resistance (Table S3). Initially, we orally gavaged arabinose-inducible pBAD-bARG$_{\text{Ser}}$ EcN (Fig. S7) into mice receiving arabinose in their drinking water (Fig. 4a). We used fecal colony plating to confirm stable GI colonization for at least 3 days (Fig. 4b), a duration sufficient for the probiotics to sense their environment and produce gas vesicles (high levels of which are reached within 24 hours of induction)[35]. We imaged the mice using a home-built ultrasound scanning system that enables rapid large-scale imaging of the abdomen (Fig. S8a), and BURST* ultrasound – a version of the BURST[43] pulse sequence that we optimized for GI probiotic imaging (as described in Methods). Subsequently, we sacrificed the animals for confirmatory ex vivo imaging of their intestines (Fig. S8b).

Scans of mice acquired one day after gavage of pBAD-bARG$_{\text{Ser}}$ EcN revealed high levels of ultrasound contrast in the cecum, which was

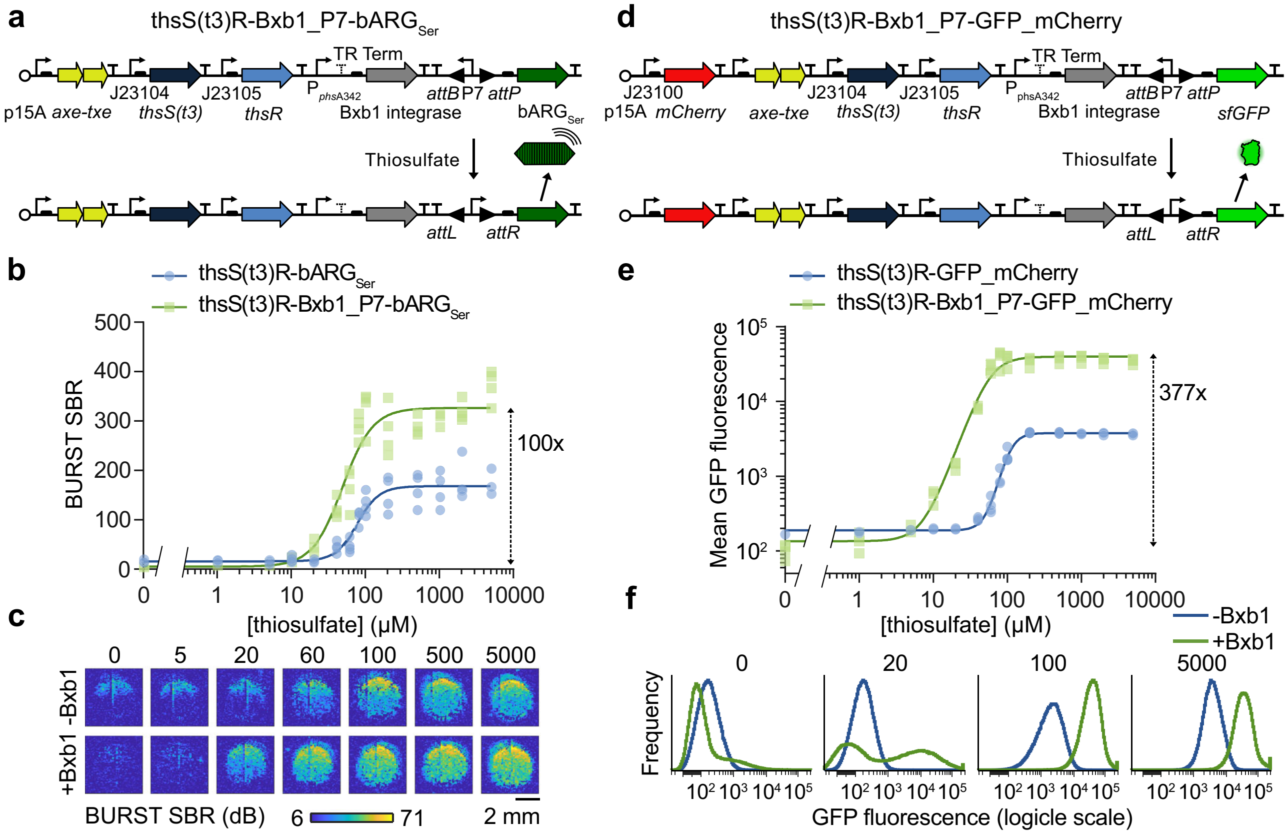

Fig. 3 | Increasing sensor activation with addition of an integrase-based switch. **a** Plasmid diagram of the optimized thiosulfate sensor thsS(t3)R-bARG$_{\mathrm{Ser}}$ with an integrase-based switch to create thsS(t3)R-Bxb1_P7-bARG$_{\mathrm{Ser}}$. Addition of thiosulfate induces expression of the Bxb1 integrase which causes irreversible site-specific recombination between the *attP* and *attB* sites that reverses the orientation of the strong constitutive P7 promoter to activate bARG$_{\mathrm{Ser}}$ expression. BURST signal-to-background ratio (SBR) (**b**) and representative images (**c**) of the optimized thiosulfate sensor with and without the Bxb1 integrase-based switch at varying thiosulfate concentrations. See Fig. S6a, b for the corresponding xAM data. **d** Plasmid diagram of the optimized thiosulfate sensor thsS(t3)R-GFP_mCherry with an integrase-based switch to create thsS(t3)R-Bxb1_P7-GFP_mCherry. Mean GFP fluorescence measured via flow cytometry (**e**) and representative histograms (**f**) of the optimized thiosulfate sensor with and without the Bxb1 integrase-based switch at varying thiosulfate concentrations. In **b** and **e**, points represent biological replicates ($N = 4$), curves represent fits to the Hill equation (see Table S2 for fitted parameters), and numbers next to dashed arrows indicate maximal fold changes. All strains were grown on plates with varying concentrations of thiosulfate at 37 °C for 20–24 hours (see Fig. S5 for images of the plates) and suspended in PBS for ultrasound imaging and flow cytometry. For ultrasound imaging, cells were cast in agarose phantoms at a concentration of 5×10^8 cells/mL. See Fig. S6c–j for the corresponding data for the tetrathionate sensor.

not present in control mice administered with the fluorescent pBAD-RFP EcN control (Fig. 4c–f, Fig. S9a). Ex vivo imaging three days after gavage confirmed that the BURST* signal was concentrated primarily in the cecum and colon (Fig. 4g–i and Fig. S9b), where resistant EcN are known to colonize in streptomycin-treated mice[31]. Signal from the colon was not as apparent in the in vivo images, likely because it was more sparse and more difficult to distinguish from background tissue, but can be better seen in 3D projections (Supplementary Videos 1-2). Negligible mutational silencing was observed in EcN plated from the feces during the course of this experiment (Fig. S9c), and EcN cells appeared to remain viable as indicated by stable colonization levels and the ability to re-express gas vesicles for ex vivo imaging after their collapse during the in vivo imaging. BURST* signal was also detected directly in feces by ultrasound imaging but was not able to be detected in mice not treated with streptomycin due to lower levels of EcN colonization (Fig. S10).

We next aimed to confirm that our thiosulfate-sensing acoustic biosensor EcN cells could be detected via ultrasound in mice directly fed with thiosulfate. After 2 days of streptomycin treatment, the thsS(t3)R-bARG$_{\mathrm{Ser}}$ and thsSR-GFP probiotics were orally administered to populate the GI tract (Fig. 4j, S11a, b). One day after gavage of the biosensors, 1 M thiosulfate was orally administered, or omitted from control mice, and the next day all mice were imaged with ultrasound. In the presence of thiosulfate, mice colonized with the probiotic acoustic biosensor exhibited significantly higher BURST* signal in the cecum compared to mice that did not receive the corresponding biomarker or were colonized by control fluorescent strains (Fig. 4k, l). The amount of contrast scaled with the amount of administered thiosulfate (Fig. S11c–e). Similar results were obtained with the tetrathionate sensor (Fig S11f, g). These results demonstrated that our probiotic EcN cells are capable of populating the mouse GI tract in vivo and functioning as acoustic biosensors of thiosulfate and tetrathionate when present at sufficient concentrations.

Streptomycin-treated mice exhibit dysbiosis-associated inflammation

To test our biosensors in a disease context, we set out to establish and validate a mouse model of inflammatory dysbiosis. Since streptomycin treatment can cause inflammation[52], we aimed to determine whether mice treated with this antibiotic exhibit elevated intestinal thiosulfate levels. Accordingly, we treated mice with streptomycin sulfate or the control antibiotic chloramphenicol for 5 days (Fig. 5a). The streptomycin-treated mice exhibited signs of dysbiosis and inflammation, including looser stools and greater weight loss compared to chloramphenicol-treated controls (on top of acute weight reduction caused by fasting with tail cups between days 2 and 3 to prevent

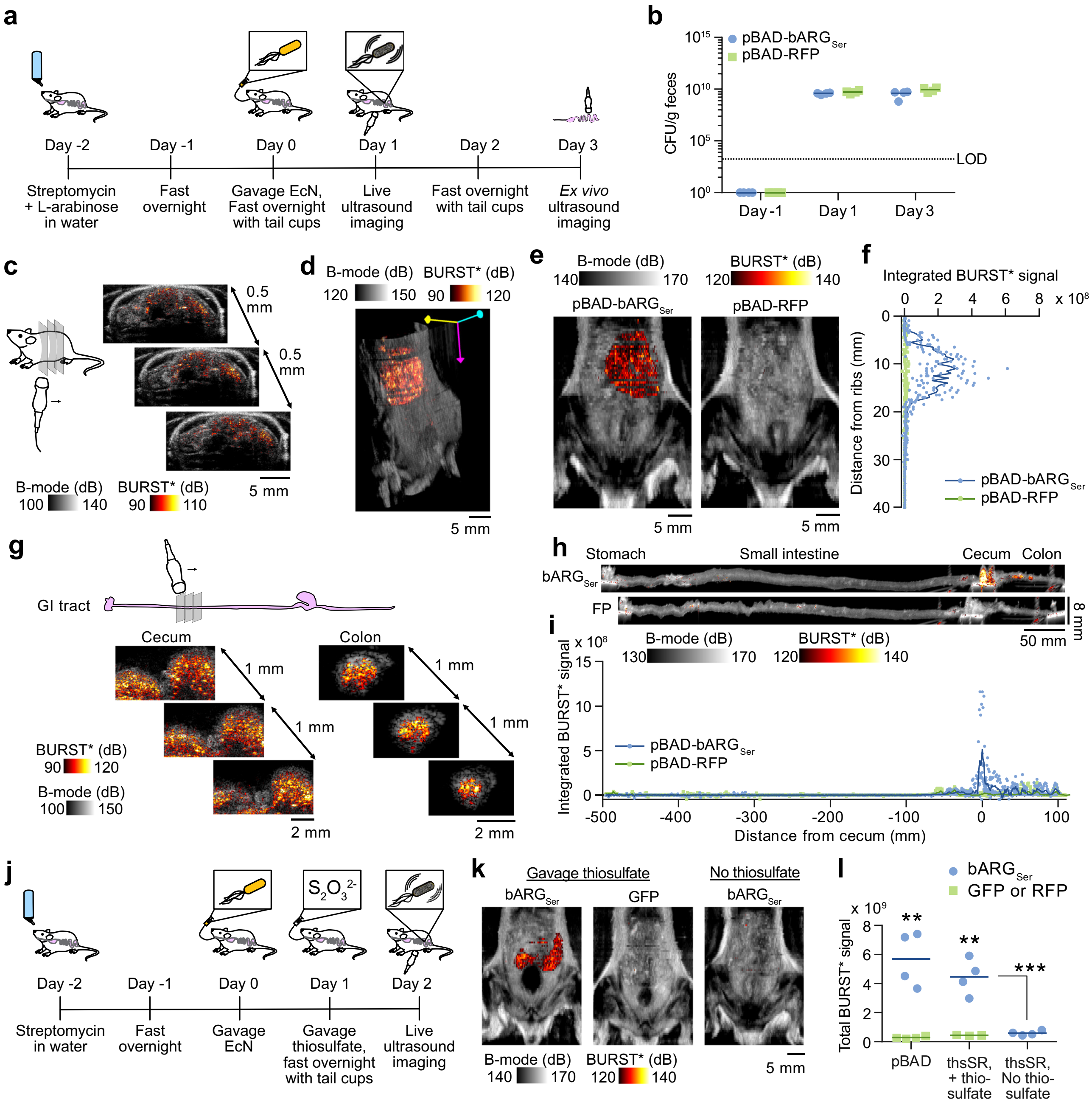

Fig. 4 | Imaging ARG expression by EcN in the GI tract in response to L-arabinose and thiosulfate. **a** Experimental design for testing L-arabinose-inducible bARG$_{Ser}$ expression in EcN in vivo. **b** Colony forming units (CFU) per gram of feces 1 day before and 1 and 3 days after administration of the EcN. LOD = limit of detection. **c** Representative 2-D images from scanning a mouse colonized by pBAD-bARG$_{Ser}$ EcN where the BURST* image (hot scale) was thresholded and overlaid onto the B-mode image (greyscale). See Fig. S8a for the imaging setup. **d** Representative 3-D projection of the BURST*/B-mode images of a mouse colonized by pBAD-bARG$_{Ser}$ EcN. See Supplementary Videos 1-2 for more views of the 3-D images. **e** Representative BURST*/B-mode images integrated over the depth on day 1. See Fig. S9a for images of all mice. **f** Integrated BURST* signal versus the distance from the ribs on day 1. **g** Representative ex vivo 2-D BURST*/B-mode images from scanning the GI tract of a mouse colonized by pBAD-bARG$_{Ser}$ EcN. See Fig. S8b for the imaging setup. **h** Representative BURST*/B-mode images integrated over the width of intestines on day 3. Note that the pixels are not isotropic. See Fig. S9b for images of all intestines. **i** Integrated BURST* signal versus the length of the intestines relative to the cecum on day 3. **j** Experimental design for testing thiosulfate-sensing EcN strains in vivo. **k** Representative integrated BURST*/B-mode images of mice colonized by thiosulfate-sensing EcN one day after oral gavage of thiosulfate, or without any external thiosulfate for control mice. See Fig. S11 for images of all mice and colonization data. **l** Total BURST* ultrasound signal in mice colonized by L-arabinose-sensing (pBAD) or thiosulfate-sensing (thsSR) EcN strains with either bARG$_{Ser}$ or GFP as the output. Asterisks represent statistical significance by two-tailed, unpaired Student's *t*-tests (** = $p < 0.01$, *** = $p < 0.001$). *p*-values from left to right: 0.00120628, 0.0026301, 0.00078501. For **b**, **f**, **i**, and **l**, each point represents a biological replicate ($N = 4$ for all except $N = 3$ for thsSR-GFP in **l**) and lines represent the mean.

coprophagy[53,54] and prepare for imaging) (Fig. 5b). Using ion chromatography-mass spectrometry (IC-MS) to quantify thiosulfate (Fig. S12), we found that fecal thiosulfate levels were elevated in streptomycin-treated mice compared to chloramphenicol-treated (Fig. 5c) or untreated (Fig. S13a, b) animals. These thiosulfate levels were higher than those measured in mice treated with dextran sulfate sodium (DSS), another agent known to cause GI inflammation[55], which was also not compatible with antibiotic treatment needed for EcN

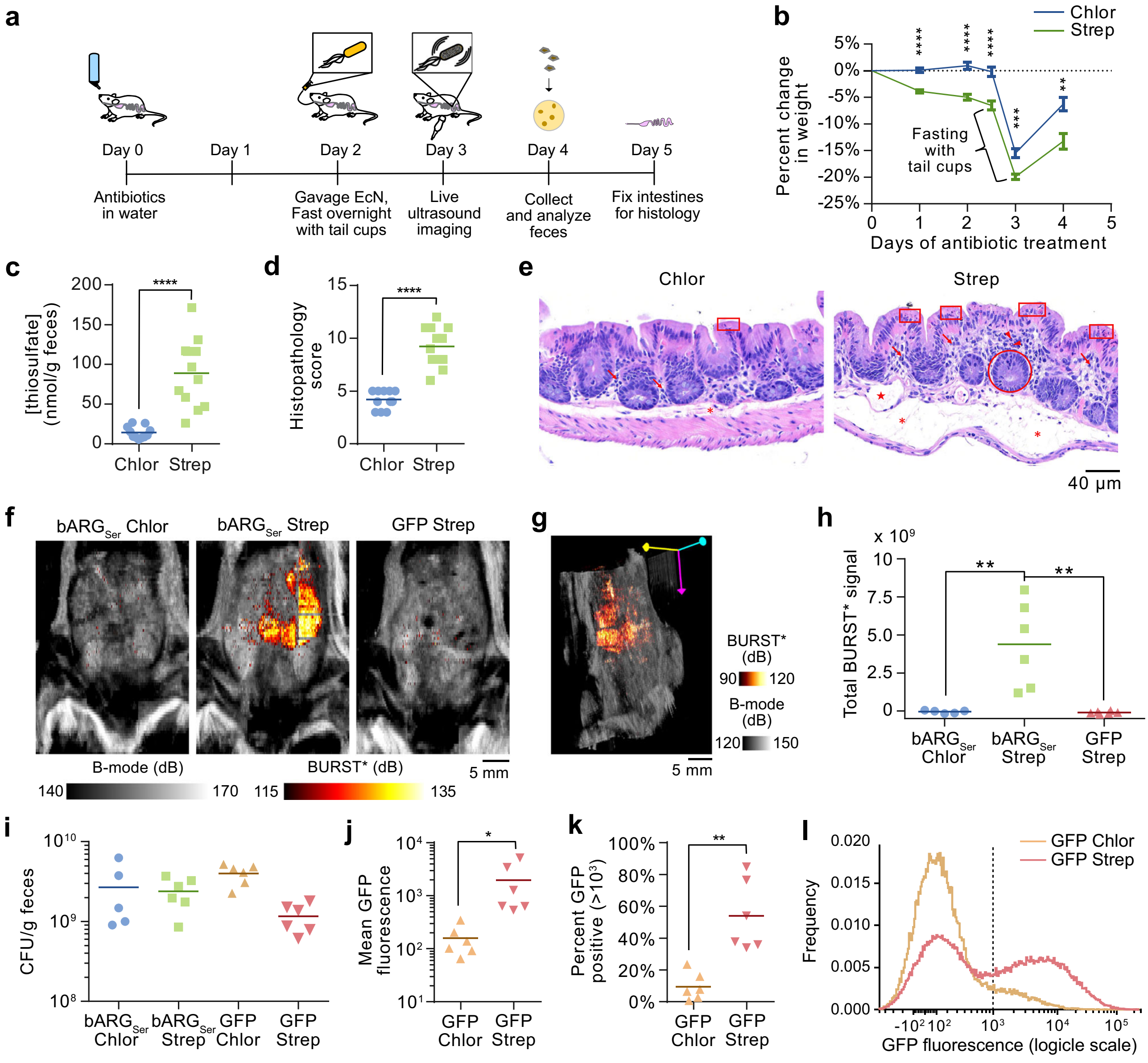

Fig. 5 | Ultrasound imaging of thiosulfate sensor activation during antibiotic-induced inflammation. **a** Experimental design for testing EcN strains with integrase-based thiosulfate sensors in antibiotic-treated mice. **b** Percent change in weight after addition of chloramphenicol (Chlor) or streptomycin (Strep) to the drinking water. *P*-values from left to right: 1.309050e-07, 7.544644e-07, 3.185578e-05, 0.000135693, 0.00171773. **c** Fecal thiosulfate concentration measured via IC-MS on day 4. See Fig. S12 for IC-MS chromatograms and standard curves. *P*-value: 1.17999e-05. Histopathology scores (**d**) and representative images (**e**) of H&E-stained sections of cecal tissue from mice sacrificed on day 5. Abnormalities are indicated in red: mucosal epithelial cell death and degeneration (box), mucosal crypt hyperplasia (circle), mucosal/submucosal edema (asterisk), mononuclear infiltrates (arrow), granulocytic infiltrates (arrowhead), dilated lymphatic (star). See Fig. S14 for the scoring by category and additional images. *P*-value: 5.38198E-08 (**d**). **f** Representative integrated BURST*/B-mode images of chloramphenicol-treated mice treated colonized with thsS(t3)R-Bxb1_P7-bARG_{Ser} EcN (bARG_{Ser} Chlor), streptomycin-treated mice colonized with thsS(t3)R-Bxb1_P7-bARG_{Ser} EcN (bARG_{Ser} Strep), and streptomycin-treated mice colonized with thsS(t3)R-Bxb1_P7-GFP_mCherry EcN (GFP Strep) on day 3. See Fig. S16 for all images. **g** Representative BURST*/B-mode 3-D projection of a bARG_{Ser} Strep mouse; see Supplementary Videos 3-5 for more views. **h** Total BURST* signal from mice imaged on day 3. *P*-values from left to right: 0.0068, 0.0029. **i** Colony forming units (CFU) per gram of feces on day 4 for mice in the groups from (**f**), plus chloramphenicol-treated mice colonized with thsS(t3)R-Bxb1_P7-GFP_mCherry EcN (GFP Chlor). Mean GFP fluorescence (**j**), percent GFP positive events ($>10^3$) (**k**), and aggregate histograms of GFP fluorescence (**l**) from flow cytometry analysis of feces from mice colonized with thsS(t3)R-Bxb1_P7-GFP_mCherry EcN on day 4. *P*-values: 0.0466 (**j**), 0.0010 (**k**). Asterisks represent statistical significance by two-tailed, unpaired Student's *t*-tests ($* = p < 0.05$, $** = p < 0.01$, $*** = p < 0.001$, $**** = p < 0.0001$). Points represent biological replicates ($N = 11$ for Chlor, $N = 12$ for Strep, $N = 5$ for bARG_{Ser} Chlor, $N = 6$ for bARG_{Ser} Strep, $N = 6$ for GFP Chlor, and $N = 6$ for GFP Strep), lines represent means, and error bars represent the standard error of the mean.

colonization (Fig. S13a, b). Given these results and difficulties in quantifying tetrathionate, we decided to focus on thiosulfate sensing in antibiotic-induced inflammation.

Blinded histological analysis of the cecal tissue from mice sacrificed after 5 days of streptomycin treatment revealed significantly more inflammatory pathology, including mononuclear infiltrates, granulocytic infiltrates, and mucosal crypt hyperplasia, compared to controls (Fig. 5d, e, Fig. S14). These results confirm that streptomycin treatment leads to intestinal dysbiosis[56] and inflammation[52] and elevates fecal thiosulfate. Quantitatively, the concentration of thiosulfate measured in the feces (~90 μM in streptomycin-treated mice, assuming an approximate density of 1 g feces per mL[57]) and initial flow cytometry measurements (Fig. S13c–e) and imaging experiments (Fig. S11h) suggested that our recombinase-based biosensors would be the most suitable agents for detecting this inflammatory process with ultrasound. When induced with 90 μM thiosulfate, the recombinase-based thiosulfate sensor was detectable with BURST imaging down to 10^5 cells/mL in vitro (Fig. S15), consistent with previous imaging results of bARG_{Ser}-expressing EcN[35]. However, as indicated by preliminary in vivo imaging experiments (Fig. S10), a concentration of >~10^8 cells/mL is likely required to see a signal above background tissue in vivo, necessitating the use of antibiotics to achieve high levels of colonization.

Probiotic acoustic biosensors enable noninvasive imaging of GI inflammation in a mouse model of inflammatory dysbiosis

To test whether our optimized thiosulfate biosensors can visualize streptomycin-induced inflammation, we orally administered the thsS(t3)R-Bxb1_P7-bARG_{Ser} and thsS(t3)R-Bxb1_P7-GFP_mCherry EcN probiotics two days after the start of dysbiosis induction (Fig. 5a). Ultrasound imaging on day 3 revealed strong BURST* signal in the cecum of streptomycin-treated mice that received the acoustic biosensor; this signal was not present in chloramphenicol-treated controls that received the same biosensor (which carries chloramphenicol resistance), nor in streptomycin-treated mice that received the fluorescent version of the sensor (Fig. 5f–h, Fig. S16, and 3D renderings in Supplementary Videos 3–5). Plating of feces on day 4 confirmed that both biosensor strains colonized streptomycin- and chloramphenicol-treated mice well (Fig. 5i). Corroborating our acoustic biosensor results, flow cytometry of the feces obtained on day 4 from mice administered with the fluorescent biosensor showed increased GFP fluorescence and a larger GFP-positive population in streptomycin-treated animals (Fig. 5j–l). The observed BURST* signal in individual animals was positively correlated with the measured weight loss and thiosulfate levels, which were themselves positively correlated with the histopathology score (Fig S17).

In separate experiments, we verified that sulfate on its own, at the same or higher level as present in our streptomycin sulfate solution, did not affect fecal thiosulfate (Fig. S18), consistent with literature[58]. When we removed the sulfate from the streptomycin sulfate solution via calcium chloride precipitation, mice receiving this sulfate-depleted streptomycin solution still exhibited BURST* signals, though these were lower than mice receiving streptomycin sulfate, with both groups exhibiting similar symptoms of inflammation, including weight loss and looser stools (Fig. S19a–f). The significantly higher BURST* signals (and GFP fluorescence) in sulfate-depleted streptomycin treated mice relative to control non-inflamed mice receiving chloramphenicol (Fig. S19d–i) indicate that thiosulfate elevation does not require sulfate administration with the dysbiosis-causing antibiotic. Together, these results suggest that although dietary sulfate alone does not cause inflammation or elevated thiosulfate, it enhances the accumulation of thiosulfate resulting from streptomycin-induced dysbiosis.

To show that our biosensing approach can be generalized beyond streptomycin, we aimed to test whether other antibiotics could cause inflammation and elevated thiosulfate. We selected piperacillin because many sulfate-reducing bacteria (SRB) are resistant to it[59,60], so it is unlikely to inhibit SRB-based sulfide generation in the GI tract which has been linked to colitis[40,61] and could contribute to intestinal thiosulfate generation[36]. We constructed a piperacillin-resistant EcN strain (Fig S20a, b), transformed it with our recombinase-based thiosulfate sensor, and showed that it activated in piperacillin-treated mice in a dose-dependent manner as indicated by the BURST* signal (Fig. S20c–f). Piperacillin-treated mice also exhibited similar levels of severity of histopathological changes associated with inflammation as streptomycin-treated mice (Fig. S20g, h). Together, these results demonstrate the in-situ activation of thiosulfate-sensing acoustic biosensors in a disease model, allowing a specific inflammatory biomarker to be imaged noninvasively with ultrasound.

Discussion

In this study, we introduced, optimized, and validated the first probiotic biosensors that can be used to visualize GI inflammation noninvasively with ultrasound. We showed that these biosensors could be imaged 1-3 days after oral administration and responded robustly to multiple compounds (arabinose, tetrathionate, thiosulfate) to produce ultrasound contrast detectable above the backdrop of intestinal tissue and luminal contents. We demonstrated that a probiotic acoustic biosensor of thiosulfate – optimized through several rounds of mutagenesis, screening, and circuit design – could be used to noninvasively visualize inflammatory dysbiosis caused by two different antibiotic treatments, with in vivo imaging data correlating with disease severity.

Because ultrasound imaging systems are relatively inexpensive and widely available[33], we anticipate that the development of ARG-producing probiotic biosensors will help facilitate the clinical adoption of “diagnostic yogurts”. Compared with current methods to diagnose and monitor IBD, such as colonoscopies and stool tests, our approach provides an alternative that is simultaneously noninvasive and in situ, bridging the gap between molecular-level information and anatomical imaging. Our approach is also highly modular, as ARGs can be coupled with virtually any transcriptional biosensor, enabling the noninvasive imaging of a wide range of disease biomarkers or other molecular species important to health. For instance, probiotic bacteria could be engineered to sense and noninvasively report on a range of important species in the GI tract, including bile acids[62,63], formate[64,65], lactate[66], and short-chain fatty acids[67], to better understand their role in health and disease or diagnose and track human conditions. However, it is important to note that the biosensing ability of the bacteria will be limited by its ability to colonize different GI regions at sufficient levels for acoustic detection.

Specific to the biosensing targets of this study, our experiments emphasize the role of antibiotics in causing dysbiosis and intestinal inflammation through host-microbial interactions[56,68–73]. Streptomycin, commonly used to assist *E. coli* colonization in rodent studies[49,50], induces mild inflammation[52] and dysbiosis[74–77] that increases intestinal thiosulfate levels, likely due to a bloom of *Enterobacteriaceae* and other facultative anaerobes which metabolize sulfomucins and sulfur-containing amino acids, producing sulfide as a byproduct that is detoxified by the host to thiosulfate[37–39,78–81]. The sulfate present in the administered streptomycin solutions enhanced intestinal thiosulfate levels in combination with streptomycin, but did not increase thiosulfate when administered alone; this is possibly because streptomycin-induced dysbiosis resulted in higher levels of SRB, which convert sulfate to sulfide and have been implicated in colitis development[82,83]. Chloramphenicol-treated mice might represent mice with a healthier GI tract by suppressing the growth of SRB[59,60] and other bacteria that contribute to sulfide generation. Overall, our results suggest that streptomycin sulfate treatment is a mouse model for dysbiosis-associated intestinal inflammation, with thiosulfate as a biomarker for disease severity. Given that DSS and piperacillin also increase intestinal thiosulfate and cause inflammation, this molecule could be a more general IBD biomarker, but future studies are needed to investigate its importance in other models of IBD and in humans and resolve the potentially confounding effects of exogeneous sulfur.

Outside of inflammatory biosensing, our results suggest that ARGs could be useful for the noninvasive study and monitoring of a larger variety of commensal microbes, pathogens, or engineered bacteria in the GI tract[84]. ARGs could be expressed in different species of bacteria to visualize their locations and gene expression over time in response to different perturbations to the GI tract. For example, to better understand the role of gut microbes in gastrointestinal cancers[85], colonization of different bacteria in tumors along the GI tract could be monitored using ARGs. Additionally, the spatiotemporal expression of virulence genes by pathogenic bacteria[86] or commensal colonization factors by commensal bacteria[87] could be noninvasively monitored by linking them with ARG expression to better understand their roles in causing GI infections or aiding colonization.

We envision several improvements to our technology. First, given the role of antibiotics in causing dysbiosis and inflammation, and regulatory concerns about the spread of antibiotic resistance, the colonization of sensor bacteria should not be dependent on antibiotic treatment. To instead obtain high levels of stable colonization of sensor bacteria, the bacteria could be engineered to metabolize an external carbon source that cannot be used by members of the native microbiome; this strategy has been successfully used in *Bacteroides* by engineering it to consume the polysaccharide porphyran[88]. Alternatively, an osmotic laxative such as PEG could be used to lower colonization resistance in addition to helping prepare the bowel for imaging[89,90]. Second, the detection of bARG_{Ser} expression in the GI tract relies on collapse of gas vesicles through BURST imaging due to the high background and non-uniformity from intestinal contents and tissue, limiting imaging sessions to at most once per day to allow time for gas vesicle re-expression. To overcome this limitation, bARG_{Ser} could be engineered to produce more nonlinear contrast that can be detected above background in the GI tract so that it can be imaged nondestructively with amplitude modulation pulse sequences[45,91]. Similar strategies could be used to improve the apparent in vivo acoustic detection limit of 10^8 CFU/g feces, which would enable imaging of strains colonizing at lower levels such as *E. coli* NGF-1 without antibiotics[25]. Additionally, to complement thiosulfate and tetrathionate, additional sensors could be engineered to sense human-validated biomarkers such as calprotectin[28,29] and tested in models of inflammation that display more localized patterns of disease, such as TNBS-induced colitis[92]. Finally, to facilitate the clinical adoption of this technology, parallel advances in ultrasound scanning technology are needed to enable volumetric imaging[93,94,95,96] or be adapted for continuous long-term disease monitoring by using adhesive ultrasound devices[97,98]. Preclinical adoption would be facilitated by greater access to automated, ready-to-use ultrasound scanning systems[99]. In either case, emerging artificial intelligence systems could greatly help with image acquisition[100] and interpretation[101–103]. With these improvements, diagnostic yogurts could become a valuable new flavor of biotechnology.

Methods

Molecular biology

All plasmids were assembled using reagents from New England Biolabs (NEB) for Gibson Assembly and from fragments generated via PCR with Q5 High Fidelity DNA polymerase (NEB). Assemblies were transformed into NEB Stable *E. coli* via electroporation for plasmid preparation and maintenance, and all plasmids were verified with commercial Sanger sequencing (Laragen) or whole-plasmid sequencing (Primordium Labs). Plasmids containing the thiosulfate and tetrathionate TCS components, pKD236-4b (encoding *thsS*), pKD237-3a-2 (encoding *thsR*), pKD238-1a (encoding *ttrS*), and pKD239-1g-2 (encoding *ttrR*), were gifts from Jeffrey Tabor (Rice University). Components for the recombinase-based switch, including Bxb1, P7, *attB*, and *attP*, were amplified from plasmids from Abedi et al.[47]. The plasmid backbone containing a chloramphenicol resistance gene and the p15A origin of replication, as well as arabinose-inducible components (*araC* and pBAD promoter), bARG_{Ser}, and Axe-Txe were amplified from plasmids from Hurt et al.[35]. The Axe-Txe stability cassette[42] enabled plasmids to be maintained without antibiotics[35], such as in vivo when different antibiotics were instead used for colonization, because the antitoxin Axe is degraded faster than the toxin Txe. The pOSIP plasmid kit used for clonetegration was a gift from Drew Endy and Keith Shearwin (Addgene kit # 1000000035). Genomic modifications to *E. coli* Nissle (EcN) were verified by colony PCR with OneTaq DNA polymerase (NEB), gel purification of bands, and sequencing (Laragen or Primordium Labs). Integrated DNA Technologies synthesized other genes and all PCR primers (see Supplementary Data for primer sequences).

Materials and media

LB media was prepared using 10 g/L Bacto tryptone (BD Biosciences), 5 g/L Bacto yeast extract (BD Biosciences), and 5 g/L NaCl; LB-agar plates were prepared with the addition of 15 g/L Bacto agar (BD Biosciences). M9 media was prepared using 1x M9 salts (Sigma-Aldrich), 0.4% v/v glycerol, 0.2% w/v Bacto casamino acids (BD Biosciences), 2 mM MgSO_4, and 0.1 mM CaCl_2; M9-agar plates were prepared with the addition of 15 g/L Bacto agar (BD Biosciences). Sodium thiosulfate pentahydrate (Sigma-Aldrich) and potassium tetrathionate (Sigma-Aldrich) solutions were freshly prepared in water and used within a day. DSS (36,000 - 50,000 MW, colitis grade, MP Biomedicals) solutions were prepared fresh every 2 days. Chloramphenicol (Sigma-Aldrich), streptomycin sulfate (Sigma-Aldrich), and piperacillin sodium salt (Cayman Chemical Company) were prepared as 1000X stock solutions and stored at -20°C for in vitro experiments or were prepared fresh for animal experiments. All other chemicals were of analytical grade and commercially available.

Mutant library generation and screening

For site-directed mutagenesis of constitutive Anderson promoters, semi-random primers (Fig. S2a) were used for PCR with Q5 High Fidelity DNA polymerase (NEB). For error-prone PCR of *thsS*, Taq DNA polymerase (NEB) with the standard reaction buffer (NEB), 0.2 mM dATP/dGTP, 1 mM dCTP/dTTP, 0.5 μM primers, 5.5 mM MgCl_2, and 0.2 mM or 0.5 mM MnCl_2 was used. After assembly via Gibson Assembly, mutant libraries were transformed via electroporation into NEB Stable *E. coli*. Various 10-fold dilutions of the outgrowth were plated onto LB-agar plates with antibiotics (30 μg/mL chloramphenicol + 100 μg/mL streptomycin) to ensure evenly spaced colonies for replica plating. Transformant colonies were transferred to M9-agar plates with antibiotics with and without the appropriate inducer (1 mM thiosulfate or tetrathionate) via replica plating, and replica plates were grown at 30 °C or 37 °C for 20–24 hours. Colonies that were more opaque or that had higher GFP expression at 1 mM than at 0 mM inducer were picked from the plate with 0 mM inducer into LB media with antibiotics and grown at 37 °C overnight. One μL of the overnight culture was then dropped onto M9-agar plates with varying thiosulfate or tetrathionate concentrations to make patches, and patch plates were grown at 30 °C or 37 °C for 20–24 hours. ARG-expressing patches were quantified in terms of opacity by acquiring white trans images with the standard filter using a Bio-Rad ChemiDoc MP gel imager. GFP-expressing patches or colonies were quantified by acquiring an image using blue epi illumination and a 530/28 filter. For quantifying patch opacity, ROIs were drawn around patches and the background directly adjacent to the patch using ImageJ. The mean pixel intensity of the background ROI next to the patch was subtracted from the mean pixel intensity of the patch ROI to correct for nonuniformity in the background of the white trans image. The background-subtracted mean pixel intensities were then normalized so that a value of 0 represented the opacity of the parent strain at 0 mM inducer and 30 °C, and a value of 1 represented the opacity of the parent strain at 1 mM inducer and 30 °C. These values were termed "relative patch opacity."

Because *E. coli* Nissle (EcN) appeared to mutate plasmids during transformation, all EcN transformants had to be screened. Sequence-verified plasmids purified from NEB Stable *E. coli* cultures were transformed into EcN via electroporation. The resulting transformant colonies were screened by streaking onto plates with antibiotics (30 μg/mL chloramphenicol, 100 μg/mL streptomycin, and/or

25 μg/mL piperacillin) and with and without the appropriate inducer (1 mM thiosulfate or tetrathionate). Only colonies which expressed GFP/bARG$_{Ser}$ on the inducer plate were picked from the plate without inducer into LB media with antibiotics. LB cultures were grown at 37 °C or 30 °C overnight, and cryostocks were prepared by gently mixing 500 μL of the overnight culture with 500 μL of 30% glycerol and placing at −80 °C.

In vitro characterizations

To characterize strains in vitro, the appropriate cryostock was used to inoculate LB + 0.4% glucose + antibiotics (30 μg/mL chloramphenicol, 100 μg/mL streptomycin, and/or 25 μg/mL piperacillin), which was grown overnight at 37 °C and 250 rpm. For characterizations in liquid culture, the overnight culture was used to inoculate 25–50 mL of M9 media + antibiotics in 250 mL baffled flasks at an initial OD$_{600}$ of 0.05 (NanoDrop 2000c, Thermo Fisher Scientific). Once the OD$_{600}$ of the M9 culture reached 0.1–0.3, 1 mL aliquots were distributed in 15 mL tubes and induced with thiosulfate, tetrathionate, or L-arabinose or left uninduced. The 1 mL cultures were grown at 37 °C and 250 rpm for 20–24 hours before being placed at 4 °C or on ice until analyzed by ultrasound imaging or flow cytometry. For characterizations on solid media, 1 μL from the overnight culture was dropped onto M9 plates + antibiotics and the desired inducer concentrations. Plates were grown at 37 °C for 20–24 hours, and the resulting patches were scraped off using inoculating loops into PBS and kept on ice or at 4 °C until ultrasound imaging or flow cytometry.

Ultrasound imaging of in vitro bacterial samples and feces

To prepare phantoms of bacterial cells for ultrasound imaging, wells were cast with a custom 3D-printed mold using 1% (w/v) agarose in PBS, which was degassed by incubating at 65–75 °C for at least 16 hours. The culture or cell suspension to be imaged was diluted to 2x the final desired cell concentration in a volume of 100 μL in PBS on ice. The 100 μL of cells in PBS was placed on a heating block at 42 °C for approximately one minute, 100 μL of molten 1% agarose in PBS at 42 °C was gently mixed in, and the mixture was pipetted into the wells of the phantom in duplicate, taking care to avoid bubbles. To prepare phantoms of feces for ultrasound imaging, 10 μL of molten 1% agarose in PBS at 55 °C was pipetted into a well, and a fecal pellet was quickly pushed into the well into the molten agarose. More molten agarose was pipetted on top of the fecal pellet to completely fill the well and any air pockets.

Once solidified, the phantoms were submerged in PBS, and ultrasound images were acquired using a MATLAB-based Verasonics Vantage programmable ultrasound scanning system and an L22-14v (Figs. 2, S1, S4, S7, S10) or an L22-14vX (Fig. 3, S6, S21) 128-element linear array transducer. The L22-14v transducer had a center frequency of 18.5 MHz with 67%-6-dB bandwidth and an elevation focus of 6 mm. The L22-14vX transducer had a center frequency of 18.0 MHz with >60%-6-dB bandwidth and an elevation focus of 8 mm. Both transducers had an element pitch of 100 μm and an elevation aperture of 1.5 mm. The transducer was attached to a custom-made manual translation stage to move between samples.

B-mode and xAM images were acquired using the same parameters as described previously[35]: the frequency and transmit focus were set to 15.625 MHz and 5 mm, respectively, and each image was an average of 50 accumulations. B-mode imaging was performed with a conventional 128-ray-lines protocol, where each ray line was a single pulse transmitted with an aperture of 40 elements. xAM imaging was performed using a custom sequence detailed previously[45] with an angle of 19.5° and an aperture of 65 elements. With the L22-14v transducer, BURST images were acquired as a series of pAM[91] images where the focus was set to 6 mm and the frequency was set to 18.0 MHz with 2 waveform cycles (3 half-cycles plus a half-cycle equalization), and the voltage was set to 1.6 V for the first 10 frames and 25 V for the last 46 frames. With the L22-14vX transducer, BURST images were acquired as a series of B-mode images, where three 32-aperture focused beams were acquired at a time to improve the frame rate by a factor of 3, and where the first image was acquired at 1.6 V and the last 7 images were acquired at 20 V. The focus was set to 6 mm and the frequency was set to 18.0 MHz with 3 half-cycles and a half-cycle equalization.

For image processing and analysis, custom beamforming scripts were applied on-line to reconstruct images from the acquired RF data. BURST images were calculated as the first collapsing frame minus the last collapsing frame (Fig S21, Supplementary Note 1). Circular ROIs were drawn around the sample wells and around the background regions in the phantom without wells in MATLAB. The signal-to-background ratio was calculated as the mean pixel intensity of the sample ROI divided by the mean pixel intensity of the background ROI. Conversion to decibels (dB) was calculated as 20*log10(SBR). For display, images were normalized by dividing by the average background signal of all images being compared and setting the lower and upper limits of the colormaps to be the same, where the lower limit was equal to a constant A and the upper limit was equal to a constant B times the maximum pixel intensity divided by the average background out of all images being compared; images were then converted to dB. For BURST images, A = 3 and B = 1 with the L22-14v transducer, and A = 2 and B = 0.5 with the L22-14vX transducer. For xAM images, A = 2 and B = 0.5 with the L22-14v transducer, and A = 2 and B = 0.4 with the L22-14vX transducer.

Animal procedures

All animal experiments were approved by the California Institute of Technology Institutional Animal Care and Use Committee (IACUC). Animals were housed in a facility maintained at 71–75°F and 30-70% humidity, with a lighting cycle of 13 hours on & 11 hours off (light cycle 6:00 AM–7:00 PM). All mice were 6-10 week-old female Balb/c (Fig. 4, S9, S10, S11, S21) or male C57BL/6 (Figure 5, S13, S14, S16, S17, S18, S19, S20) mice obtained from Jackson Labs. For antibiotic, DSS, and inducer treatments administered in the drinking water *ad libitum*, the appropriate compounds were dissolved in water and filtered with a 0.2 μm membrane; the water was freshly prepared at least every 2 days. Antibiotics were maintained in the water throughout the course of the experiment when provided. Standard rodent diet (5053 - PicoLab Rodent Diet 20) was provided *ad libitum* unless mice were being fasted. Oral gavage was performed using a 20 gauge 1.5″ length animal feeding needle and with a volume of 200 uL. Prior to gavage, mice were fasted in individual housing for 2–3 hours. EcN strains were prepared for gavage by growing an overnight culture in LB + 0.4% glucose + antibiotics at 37°C from a cryostock, diluting the overnight culture 1:100 into 50 mL of fresh M9 or LB + 0.4% glucose + antibiotics in 250 mL baffled flasks, incubating at 37 °C and 250 rpm until the OD$_{600}$ reached 0.4–0.6, pelleting the culture at 3500 g at room temperature for 10 min, and suspending in an appropriate volume of sterile PBS for an OD$_{600}$ of 20. Feces were collected by placing mice individually in empty cages without food or bedding for approximately 20–30 minutes.

In vivo ultrasound imaging

Prior to imaging, mice were fasted overnight with tail cups, which prevent coprophagy[53], in individual housing with access to water only to reduce the amount of material and background ultrasound signal in the GI tract[54], in addition to preventing re-ingestion of EcN, which would confound the imaging results. Shortly before imaging, mice were anesthetized with 2% isoflurane, the tail cups were removed, and the abdominal fur was removed with shaving and Nair. Approximately 5 minutes before imaging, 1.2 μg atropine in a volume of 60 μL saline was injected subcutaneously on each side of the abdomen to slow movement of intestines due to peristalsis[104,105]. Mice were placed prone and partially submerged in water onto a thin film of mylar (2.5 μm thickness, Chemplex, catalog number 100) which was acoustically transparent. A nose cone provided isoflurane and kept the head out of the water, white a heating lamp was used to regulate the body temperature. The ultrasound transducer (L22-14v or L22-14vX) was submerged using a probe cover (Protek, part number 1-519-2450) and attached to a BiSlide computer-controlled 3-D translatable stage (Velmex). The transducer was positioned 6 mm below the mylar at an angle of 15° from the vertical to minimize specular reflection, and at a distance from the mylar to center the 6 mm focus on the intestines. See Fig. S8a for a diagram.

A custom MATLAB script was used to control the ultrasound system and the 3-D translatable stage at the same time so that the entire abdominal area of the mouse was automatically scanned. Starting at the rib cage, the transducer was moved in three 9.6-mm steps across the body and in eighty 0.5-mm steps lengthwise down the body to the tail. At each spot, BURST imaging was performed, giving a total of 240 BURST acquisitions per mouse which took around 15 min to acquire. BURST acquisitions were a series of B-mode images, where three 32-aperture focused beams were acquired at a time to improve the frame rate by a factor of three[43], with the first image taken at 1.6 V and the last seven images taken at the collapsing voltage. The focus was set to 6 mm and the frequency was set to 18.0 MHz. With the L22-14v transducer (used for in vivo data in Figs. 4, S9, S11, and S21), 3 transmit waveform cycles were used and the collapsing voltage was 25 V. With the L22-14vX transducer (used for in vivo data in Figs. 5, S16, S17, S19, and S20), 2 transmit waveform cycles were used and the collapsing voltage was 20 V due to its higher pressure-to-voltage curve.

BURST* images were calculated by subtracting the first collapsing frame from the second because the ARG-specific signal was characterized by an increase in signal from the first to the second collapsing frame and using more frames was confounded by tissue motion (Fig. S21, Supplementary Note 1). Acquisitions during which breathing occurred were manually excluded. The first collapsing frame was used for the B-mode images. At each transverse plane, the three acquisitions across the body were stitched together to form one B-mode image and ROIs were drawn around the GI tract in each transverse plane B-mode image. 3-D BURST* and 3-D B-mode images were formed by stitching all 240 acquisitions together. For 3-D BURST* images, pixels were set to zero anywhere breathing occurred or outside of the ROIs. For display in 3-D, 3-D BURST* and 3-D B-mode arrays were converted to dB and loaded into napari[106] where the BURST* image rendering and blending was set to "additive." For display in 2-D, the B-mode signal was summed over the depth of the mouse from 4 to 8 mm, and the BURST* signal was summed over the depth of the entire ROI. The 2-D integrated BURST* image was thresholded, converted to dB, and overlaid onto the dB-converted 2-D integrated B-mode image. To calculate the total BURST* signal, all pixel intensities in the 3-D BURST* array inside the ROI excluding breathing were summed.

Ex vivo ultrasound imaging

Prior to imaging, mice were fasted overnight with tail cups in individual housing with access to water only to reduce the amount of material and background ultrasound signal in the GI tract. Mice were euthanized by sedating with isoflurane and performing cervical dislocation, and the entire GI tract (stomach to rectum) was quickly removed and linearized by removing mesenteric tissue, taking care not to rip the intestines. The intestines were submerged in a degassed water bath where the stomach, cecum, and rectum were pinned down on platforms so that the entire GI tract was in approximately a straight line at constant depth. The platforms consisted of acoustic absorbers (Precision acoustics) on top and magnets embedded into the platforms on the bottom so that the platforms would stay submerged and could be moved to stretch out the intestines (whose length varied between mice) using another external magnet on the bottom of the water bath. The L22-14v ultrasound transducer was attached to a BiSlide computer-controlled 3-D translatable stage (Velmex) and was positioned 8 mm above the intestines at an angle of 15° from the vertical to minimize specular reflection. See Fig. S8b for a diagram.

A custom MATLAB script was used to control the ultrasound system and the 3-D translatable stage at the same time so that the entire GI tract was automatically scanned. Starting at the stomach, the transducer was moved in approximately six hundred 1-mm steps lengthwise down to the rectum, which took around 30 min. At each spot, BURST acquisitions were obtained as a series of B-mode images, where three 32-aperture focused beams were acquired at a time to improve the frame rate by a factor of 3, with the first image taken at 1.6 V and the last seven images taken at 25 V. The focus was set to 8 mm and the frequency was set to 18.0 MHz with 3 transmit waveform cycles.

As with the in vivo images, ex vivo BURST* images were calculated by subtracting the first collapsing frame from the second (Fig. S21, Supplementary Note 1), and the first collapsing frame was used for the B-mode images. For display in 2-D, both BURST* and B-mode images were summed over the width of the transducer (9.6 mm). The 2-D integrated BURST* image was thresholded, converted to dB, and overlaid onto the dB-converted 2-D integrated B-mode image. To calculate the integrated BURST* signal along the length of the GI tract, all BURST* pixel intensities were summed between a depth of 4 and 12 mm.

Processing fecal samples for downstream analysis

Approximately 50-150 mg of feces were collected per mouse and were stored on ice immediately after collection. Feces were homogenized at 100 mg feces per mL in sterile ice-cold PBS using vortexing and an MP Biomedical FastPrep 24 Tissue Homogenizer set to 5 m/s for 20–40 seconds. One hundred μL of the homogenized feces were saved for plating, 100–200 μL were saved for flow cytometry, and the rest were centrifuged at 10,000 *g* and 4 °C for 20 min. The supernatant was filtered through a 0.2 μm cellulose acetate membrane and was frozen at -80°C until analysis via IC-MS. The 100–200 μL that were saved for flow cytometry were mixed 1:1 with PBS containing 2 mg/mL chloramphenicol, filtered through a 40 μm membrane (Falcon Cell Strainers), and incubated at 37 °C and 250 rpm for one hour to allow fluorophore maturation while protein synthesis was inhibited by the 1 mg/mL chloramphenicol[24]. The mixture was then stored at 4 °C until analysis via flow cytometry within 24 hours. The 100 μL that was saved for plating was diluted in 900 μL sterile PBS, and five more 10-fold serial dilutions were made and plated on agar plates with antibiotics (30 μg/mL chloramphenicol, 100 μg/mL streptomycin, and/or 25 μg/mL piperacillin) and with and without inducers (1 mM thiosulfate, 1 mM tetrathionate, or 0.1% L-arabinose) using the drop plate method[107]. Total colony counts were used to calculate colony forming units (CFUs) per gram of feces, and the number of colonies that failed to express reporter genes on plates with inducer was used to calculate the fraction mutant colonies.

Flow cytometry

A MACSQuant VYB flow cytometer (Miltenyi Biotec) was used for all flow cytometry analysis with the following settings: low flow rate, medium mixing, 25–50 μL uptake volume, standard mode, chilled 96 rack, and a trigger by SSC with a threshold of 2.0. The Y2 channel was used for mCherry and the B1 channel was used for GFP. For analyzing in vitro samples, appropriate dilutions in PBS + 0.5% (w/v) BSA + 1 mg/mL chloramphenicol were prepared to target 10^6 cells/mL. For analyzing fecal samples, the 50 mg/mL feces + 1 mg/mL chloramphenicol in PBS samples that were stored at 4 °C were diluted to 2.5 mg/mL feces in PBS + 0.5% (w/v) BSA + 1 mg/mL chloramphenicol (1/20 dilution). Cytoflow[108] was used with custom Python scripts for flow cytometry data analysis. Events were gated on FSC-A and SSC-A characteristics of *E. coli* and on positive mCherry fluorescence (see Fig. S22). The geometric mean was used to calculate mean GFP fluorescence, and the fraction of GFP-positive cells was calculated as the number of events above 1000 in the B1 channel divided by the total number of gated events. For histograms, the number of bins was calculated according to the Freedman-Diaconis rule (with a minimum of 100 bins) and a logicle scale with parameters from Cytoflow was used for the x-axis.

Ion chromatography mass spectrometry (IC-MS)

Thiosulfate was quantified via IC-MS using a Dionex Integrion HPIC system coupled to an ISQ EC Single Quadrupole Mass Spectrometer (Thermo Scientific). A Dionex AS-AP autosampler was used to inject 5 µL of sample into a 25 µL sample loop in push-partial mode. Ion chromatography was performed using a Dionex IonPac AS18 analytical column (2 x 250 mm) with a guard column (2 x 50 mm) at a flow rate of 0.25 mL/min. An eluent generator (with Dionex Cartridge EGC 500 KOH) was used to create the following KOH gradient: 12 to 44 mM from 0–5 min, 44 mM from 5–8 min, 44 to 52 mM from 8–10 min, 52 mM from 10–15 min, 52 to 12 mM from 15–15.05 min, and 12 mM from 15.05–22 min. A Dionex 2 mm AERS suppressor operated at 33 mA was used to remove the KOH before conductivity detection and negative ion mode mass spectrometry. The mass spectrometer was operated in component mode to scan for thiosulfate at $m/z = 113$ using a source CID voltage of 10.

Thiosulfate standards were freshly prepared at concentrations ranging from 100 to 3000 nM in water with 1/10x PBS. The 100 mg/mL fecal filtrates in PBS to be analyzed with IC-MS were removed from −80°C, rapidly thawed in a room temperature water bath, and diluted 1/10 in water. Peaks were automatically integrated using Chromeleon 7.2.10 software with the Chromeleon 6 detection algorithm and custom parameters. Because all samples contained the same PBS concentration (1/10x), phosphate which was detected via conductivity was used as an internal standard; the thiosulfate peak area was normalized by the phosphate peak area to correct for variations in sampler injection volume. For each biological replicate, 3 technical replicates were analyzed and the mean was used for plotting.

Sulfate depletion and quantification

Sulfate was depleted from streptomycin sulfate solutions via calcium precipitation. Five grams of streptomycin sulfate was dissolved in 25 mL DI water, and 3.09 g calcium chloride dihydrate was added, causing a white precipitate of calcium sulfate to form. After 5 mins of stirring at room temperature, the precipitate was filtered off using Whatman filter paper (grade 3) and the solution was immediately diluted to 1 L in DI water because streptomycin is not stable in solution at high concentrations[109]. This streptomycin calcium chloride solution was filtered through a 0.22 µm membrane to sterilize and stored at 4 °C until administered to mice. Sulfate was quantified using a QuantiChrom™ Sulfate Assay Kit (DSFT-200, BioAssay Systems) according to the manufacturer's instructions.

Histology of cecal tissue

Mice were euthanized by sedating with isoflurane and performing cervical dislocation. The GI tract was quickly removed and a portion of the cecum was excised, flushed with ice-cold PBS to remove the contents, and fixed in 10% neutral buffered formalin for 24 hours at 4 °C. Fixed cecal tissues were transferred to 70% ethanol and stored at 4°C until being shipped to IDEXX Laboratories for paraffin-embedding, sectioning, and H&E staining. A pathologist performed blinded grading of microscopic changes twice independently as to severity using the International Harmonization of Nomenclature and Diagnostic (INHAND) Criteria grading system where 0 = no significant change, 1 = minimal, 2 = mild, 3 = moderate, and 4 = severe[110].

Structural predictions

3D models for *thsS* and *thsS(t3)* were generated from their amino acid sequences using AlphaFold 3 ref. 111 using a seed value of 100. Structures were displayed and aligned using ChimeraX[112].

Statistics and reproducibility

Sample sizes are indicated in figure captions and were chosen based on preliminary experiments to provide sufficient power for statistical comparison. Prism (version 6, GraphPad) was used to calculate *p*-values. No replicates were excluded, but BURST ultrasound acquisitions which captured breathing movements for portions of in vivo GI scans were excluded from downstream analyses; no other data were excluded. For in vivo experiments, animals were randomly distributed into cages that were randomly chosen for different conditions. For non-animal experiments, randomization was not necessary because samples being compared received the same treatments. For histological analyses, an external pathologist performed blinded grading of tissue samples. For other analyses, blinding was not necessary because data collection, processing, and analysis methods were quantitative and identical across experimental groups.

Reporting summary

Further information on research design is available in the Nature Portfolio Reporting Summary linked to this article.

Data availability

Plasmids will be made available through Addgene upon publication (Addgene IDs 232468 – 232475). All data are available within the article, its Supplementary Information, and the Source Data file. Raw unprocessed data and other materials are available upon request from the corresponding author. Source data are provided with this paper.

Code availability

Ultrasound data acquisition and analysis code are available on the Shapiro Lab GitHub at https://github.com/shapiro-lab in the "Probiotic-GI-Imaging" repository[113]. Source data are provided with this paper.

References

1. Talley, N. J. et al. An evidence-based systematic review on medical therapies for inflammatory bowel disease. *Am. J. Gastroenterol.* **106**, S2–S25 (2011).
2. Wang, R., Li, Z., Liu, S. & Zhang, D. Global, regional and national burden of inflammatory bowel disease in 204 countries and territories from 1990 to 2019: a systematic analysis based on the Global Burden of Disease Study 2019. *BMJ Open* **13**, e065186 (2023).
3. Kahn-Boesel, O., Cautha, S., Ufere, N. N., Ananthakrishnan, A. N. & Kochar, B. A Narrative review of financial burden, distress, and toxicity of inflammatory bowel diseases in the United States. *Off. J. Am. Coll. Gastroenterol. ACG* **118**, 1545 (2023).
4. Le Berre, C. et al. Impact of inflammatory bowel diseases on working life: A French nationwide survey. *Dig. Liver Dis.* **51**, 961–966 (2019).
5. Dalal, S. R. & Chang, E. B. The microbial basis of inflammatory bowel diseases. *J. Clin. Invest.* **124**, 4190–4196 (2014).
6. Baumgart, D. C. & Carding, S. R. Inflammatory bowel disease: cause and immunobiology. *Lancet* **369**, 1627–1640 (2007).
7. Buisson, A. et al. Comparative acceptability and perceived clinical utility of monitoring tools: a nationwide survey of patients with inflammatory bowel disease. *Inflamm. Bowel Dis.* **23**, 1425–1433 (2017).
8. Hong, Z. et al. Delayed diagnosis is associated with early and emergency need for first Crohn's Disease-Related Intestinal Surgery. *Med. Sci. Monit.* **23**, 4841–4846 (2017).

9. Lee, D. et al. Diagnostic delay in inflammatory bowel disease increases the risk of intestinal surgery. *World J. Gastroenterol.* **23**, 6474–6481 (2017).
10. Safroneeva, E. et al. Impact of the early use of immunomodulators or TNF antagonists on bowel damage and surgery in Crohn's disease. *Aliment. Pharmacol. Ther.* **42**, 977–989 (2015).
11. Chhaya, V. et al. Impact of early thiopurines on surgery in 2770 children and young people diagnosed with inflammatory bowel disease: a national population-based study. *Aliment. Pharmacol. Ther.* **42**, 990–999 (2015).
12. Magro, F. et al. Is it possible to change phenotype progression in Crohn's disease in the era of immunomodulators? predictive factors of phenotype progression. *J. Am. Coll. Gastroenterol. ACG* **109**, 1026 (2014).
13. Probert, C. S. J., Dignass, A. U., Lindgren, S., Oudkerk Pool, M. & Marteau, P. Combined oral and rectal mesalazine for the treatment of mild-to-moderately active ulcerative colitis: Rapid symptom resolution and improvements in quality of life. *J. Crohns Colitis* **8**, 200–207 (2014).
14. Berg, D. R., Colombel, J.-F. & Ungaro, R. The role of early biologic therapy in inflammatory bowel disease. *Inflamm. Bowel Dis.* **25**, 1896–1905 (2019).
15. Derkacz, A., Olczyk, P. & Komosinska-Vassev, K. Diagnostic markers for nonspecific inflammatory bowel diseases. *Dis. Markers* **2018**, 7451946 (2018).
16. Nikolaus, S. & Schreiber, S. Diagnostics of inflammatory bowel disease. *Gastroenterology* **133**, 1670–1689 (2007).
17. Haisma, S.-M., van Rheenen, P. F., Wagenmakers, L. & Muller Kobold, A. Calprotectin instability may lead to undertreatment in children with IBD. *Arch. Dis. Child.* **105**, 996–998 (2020).
18. Shi, J.-T. et al. Diagnostic utility of non-invasive tests for inflammatory bowel disease: an umbrella review. *Front. Med.* **9**, 920732 (2022).
19. Dolinger, M. T. & Kayal, M. Intestinal ultrasound as a non-invasive tool to monitor inflammatory bowel disease activity and guide clinical decision making. *World J. Gastroenterol.* **29**, 2272–2282 (2023).
20. Blackwell, J. et al. Prevalence and duration of gastrointestinal symptoms before diagnosis of inflammatory bowel disease and predictors of timely specialist review: a population-based study. *J. Crohns Colitis* **15**, 203–211 (2021).
21. Riglar, D. T. & Silver, P. A. Engineering bacteria for diagnostic and therapeutic applications. *Nat. Rev. Microbiol.* **16**, 214–225 (2018).
22. Landry, B. P. & Tabor, J. J. Engineering diganostic and therapeutic gut bacteria. *Microbiol. Spectr.* **5**, BAD-0020–2017 (2017).
23. Barra, M., Danino, T. & Garrido, D. Engineered probiotics for detection and treatment of inflammatory intestinal diseases. *Front. Bioeng. Biotechnol.* **8**, 265 (2020).
24. Daeffler, K. N. et al. Engineering bacterial thiosulfate and tetrathionate sensors for detecting gut inflammation. *Mol. Syst. Biol.* **13**, 923 (2017).
25. Riglar, D. T. et al. Engineered bacteria function in the mammalian gut as long term live diagnostics of inflammation. *Nat. Biotechnol.* **35**, 653–658 (2017).
26. Archer, E. J., Robinson, A. B. & Süel, G. M. Engineered Ecoli that detect and respond to gut inflammation through nitric oxide sensing. *ACS Synth. Biol.* **1**, 451–457 (2012).
27. Chen, X. J., Wang, B., Thompson, I. P. & Huang, W. E. Rational design and characterization of nitric oxide biosensors in *E. coli* Nissle 1917 and Mini SimCells. *ACS Synth. Biol.* **10**, 2566–2578 (2021).
28. Xia, J. Y. et al. Engineered calprotectin-sensing probiotics for IBD surveillance in humans. *Proc. Natl. Acad. Sci.* **120**, e2221121120 (2023).
29. Zhu, D. et al. Microbial Biosensor for Sensing and Treatment of Intestinal Inflammation. *Adv. Sci. (Weinh.)* **12**, 2504364 (2025).
30. Mimee, M. et al. An ingestible bacterial-electronic system to monitor gastrointestinal health. *Science* **360**, 915–918 (2018).
31. Foucault, M.-L., Thomas, L., Goussard, S., Branchini, B. R. & Grillot-Courvalin, C. In vivo bioluminescence imaging for the study of intestinal colonization by Escherichia coli in mice. *Appl. Environ. Microbiol.* **76**, 264–274 (2010).
32. Piraner, D. I. et al. Going deeper: biomolecular tools for acoustic and magnetic imaging and control of cellular function. *Biochemistry* **56**, 5202–5209 (2017).
33. Wang, S., Hossack, J. A. & Klibanov, A. L. From anatomy to functional and molecular biomarker imaging, and therapy: ultrasound is safe, ultrafast, portable, and inexpensive. *Invest. Radiol.* **55**, 559–572 (2020).
34. Bourdeau, R. W. et al. Acoustic reporter genes for noninvasive imaging of microbes in mammalian hosts. *Nature* **553**, 86–90 (2018).
35. Hurt, R. C. et al. Genomically mined acoustic reporter genes for real-time in vivo monitoring of tumors and tumor-homing bacteria. *Nat. Biotechnol.* **41**, 919–931 (2023).
36. Levitt, M. D., Furne, J., Springfield, J., Suarez, F. & DeMaster, E. Detoxification of hydrogen sulfide and methanethiol in the cecal mucosa. *J. Clin. Invest.* **104**, 1107–1114 (1999).
37. Blachier, F. et al. Production of hydrogen sulfide by the intestinal microbiota and epithelial cells and consequences for the colonic and rectal mucosa. *Am. J. Physiol. -Gastrointest. Liver Physiol.* **320**, G125–G135 (2021).
38. Mottawea, W. et al. Altered intestinal microbiota–host mitochondria crosstalk in new onset Crohn's disease. *Nat. Commun.* **7**, 13419 (2016).
39. Carbonero, F., Benefiel, A. C., Alizadeh-Ghamsari, A. H. & Gaskins, H. R. Microbial pathways in colonic sulfur metabolism and links with health and disease. *Front. Physiol.* **3**, 448 (2012).
40. Rowan, F. E., Docherty, N. G., Coffey, J. C. & O'Connell, P. R. Sulphate-reducing bacteria and hydrogen sulphide in the aetiology of ulcerative colitis. *Br. J. Surg.* **96**, 151–158 (2009).
41. Winter, S. E. et al. Gut inflammation provides a respiratory electron acceptor for Salmonella. *Nature* **467**, 426–429 (2010).
42. Grady, R. & Hayes, F. Axe–Txe, a broad-spectrum proteic toxin–antitoxin system specified by a multidrug-resistant, clinical isolate of Enterococcus faecium. *Mol. Microbiol.* **47**, 1419–1432 (2003).
43. Sawyer, D. P. et al. Ultrasensitive ultrasound imaging of gene expression with signal unmixing. *Nat. Methods* **18**, 945–952 (2021).
44. Landry, B. P., Palanki, R., Dyulgyarov, N., Hartsough, L. A. & Tabor, J. J. Phosphatase activity tunes two-component system sensor detection threshold. *Nat. Commun.* **9**, 1433 (2018).
45. Maresca, D., Sawyer, D. P., Renaud, G., Lee-Gosselin, A. & Shapiro, M. G. Nonlinear X-Wave Ultrasound Imaging of Acoustic Biomolecules. *Phys. Rev. X* **8**, 041002 (2018).
46. Mutalik, V. K. et al. Precise and reliable gene expression via standard transcription and translation initiation elements. *Nat. Methods* **10**, 354–360 (2013).
47. Abedi, M. H. et al. Ultrasound-controllable engineered bacteria for cancer immunotherapy. *Nat. Commun.* **13**, 1585 (2022).
48. Hentges, D. J., Pongpech, P. & Que, J. U. Hypothesis: How Streptomycin treatment compromises colonisation resistance against enteric pathogens in mice. *Microb. Ecol. Health Dis.* **3**, 105–111 (1990).
49. Leatham, M. P. et al. Precolonized Human Commensal Escherichia coli strains serve as a barrier to E. coli O157:H7 Growth in the Streptomycin-Treated Mouse Intestine. *Infect. Immun.* **77**, 2876–2886 (2009).

50. Maltby, R., Leatham-Jensen, M. P., Gibson, T., Cohen, P. S. & Conway, T. Nutritional basis for colonization resistance by human commensal Escherichia coli Strains HS and Nissle 1917 against E. coli O157:H7 in the Mouse Intestine. *PLoS ONE* **8**, e53957 (2013).
51. Myhal, M. L., Laux, D. C. & Cohen, P. S. Relative colonizing abilities of human fecal and K 12 strains of Escherichia coli in the large intestines of streptomycin-treated mice. *Eur. J. Clin. Microbiol.* **1**, 186–192 (1982).
52. Spees, A. M. et al. Streptomycin-Induced Inflammation Enhances Escherichia coli Gut Colonization Through Nitrate Respiration. *mBio* **4**, e00430-13 (2013).
53. Bogatyrev, S. R., Rolando, J. C. & Ismagilov, R. F. Self-reinoculation with fecal flora changes microbiota density and composition leading to an altered bile-acid profile in the mouse small intestine. *Microbiome* **8**, 19 (2020).
54. Buss, M. T., Ramesh, P., English, M. A., Lee-Gosselin, A. & Shapiro, M. G. Spatial Control of Probiotic Bacteria in the Gastrointestinal Tract Assisted by Magnetic Particles. *Adv. Mater*. **33**, 2007473 (2021).
55. Chassaing, B., Aitken, J. D., Malleshappa, M. & Vijay-Kumar, M. Dextran Sulfate Sodium (DSS)-Induced Colitis in Mice. *Curr. Protoc. Immunol.* **104**, 1–15 (2014).
56. Strati, F. et al. Antibiotic-associated dysbiosis affects the ability of the gut microbiota to control intestinal inflammation upon fecal microbiota transplantation in experimental colitis models. *Microbiome* **9**, 39 (2021).
57. Yang, P. J., LaMarca, M., Kaminski, C., Chu, D. I. & Hu, D. L. Hydrodynamics of defecation. *Soft Matter* **13**, 4960–4970 (2017).
58. Deplancke, B. et al. Gastrointestinal and microbial responses to sulfate-supplemented drinking water in mice. *Exp. Biol. Med.* **228**, 424–433 (2003).
59. Nakao, K. et al. Susceptibilities of 23 Desulfovibrio Isolates from Humans. *Antimicrob. Agents Chemother.* **53**, 5308–5311 (2009).
60. Lozniewski, A., Labia, R., Haristoy, X. & Mory, F. Antimicrobial susceptibilities of clinical Desulfovibrio Isolates. *Antimicrob. Agents Chemother.* **45**, 2933–2935 (2001).
61. Gibson, G. R., Cummings, J. H. & Macfarlane, G. T. Growth and activities of sulphate-reducing bacteria in gut contents of healthy subjects and patients with ulcerative colitis. *FEMS Microbiol. Lett.* **86**, 103–111 (1991).
62. Keely, S. J. et al. Contributions of bile acids to gastrointestinal physiology as receptor agonists and modifiers of ion channels. *Am. J. Physiol. - Gastrointest. Liver Physiol.* **322**, G201–G222 (2022).
63. Khodakivskyi, P. V. et al. Noninvasive imaging and quantification of bile salt hydrolase activity: From bacteria to humans. *Sci. Adv.* **7**, eaaz9857 (2021).
64. Hughes, E. R. et al. Microbial respiration and formate oxidation as metabolic signatures of inflammation-associated dysbiosis. *Cell Host Microbe* **21**, 208–219 (2017).
65. Dacquay, L. C. et al. E.coli Nissle increases transcription of flagella assembly and formate hydrogenlyase genes in response to colitis. *Gut Microbes* **13**, 1994832 (2021).
66. Remund, B., Yilmaz, B. & Sokollik, C. D-Lactate: Implications for Gastrointestinal Diseases. *Children* **10**, 945 (2023).
67. van der Hee, B. & Wells, J. M. Microbial regulation of host physiology by short-chain fatty acids. *Trends Microbiol* **29**, 700–712 (2021).
68. Tong, G. et al. Establishment and evaluation of a specific antibiotic-induced inflammatory bowel disease model in rats. *PLOS ONE* **17**, e0264194 (2022).
69. Zeng, M. Y., Inohara, N. & Nuñez, G. Mechanisms of inflammation-driven bacterial dysbiosis in the gut. *Mucosal Immunol.* **10**, 18–26 (2017).
70. Ramirez, J. et al. Antibiotics as major disruptors of gut microbiota. *Front. Cell. Infect. Microbiol.* **10**, 572912 (2020).
71. Hviid, A., Svanström, H. & Frisch, M. Antibiotic use and inflammatory bowel diseases in childhood. *Gut* **60**, 49–54 (2011).
72. Faye, A. S. et al. Antibiotic use as a risk factor for inflammatory bowel disease across the ages: a population-based cohort study. *Gut* **72**, 663–670 (2023).
73. Jin, Y. et al. From the cover: exposure to oral antibiotics induces gut microbiota dysbiosis associated with lipid metabolism dysfunction and low-grade inflammation in mice. *Toxicol. Sci.* **154**, 140–152 (2016).
74. Sekirov, I. et al. Antibiotic-Induced Perturbations of the Intestinal Microbiota Alter Host Susceptibility to Enteric Infection. *Infect. Immun.* **76**, 4726–4736 (2008).
75. Rivera-Chávez, F. et al. Depletion of butyrate-producing Clostridia from the gut microbiota drives an aerobic luminal expansion of Salmonella. *Cell Host Microbe* **19**, 443–454 (2016).
76. Kelly, C. J. et al. Crosstalk between Microbiota-derived short-chain fatty acids and intestinal epithelial HIF augments tissue barrier function. *Cell Host Microbe* **17**, 662–671 (2015).
77. Rivera-Chávez, F., Lopez, C. A. & Bäumler, A. J. Oxygen as a driver of gut dysbiosis. *Free Radic. Biol. Med.* **105**, 93–101 (2017).
78. Baldelli, V., Scaldaferri, F., Putignani, L. & Del Chierico, F. The Role of Enterobacteriaceae in Gut Microbiota Dysbiosis in Inflammatory Bowel Diseases. *Microorganisms* **9**, 697 (2021).
79. Antunes, L. C. M. et al. Effect of antibiotic treatment on the intestinal metabolome. *Antimicrob. Agents Chemother.* **55**, 1494–1503 (2011).
80. Richie, T. G. et al. Limitation of amino acid availability by bacterial populations during enhanced colitis in IBD mouse model. *mSystems* **8**, e00703-23 (2023).
81. Barton, L. L., Ritz, N. L., Fauque, G. D. & Lin, H. C. Sulfur Cycling and the Intestinal Microbiome. *Dig. Dis. Sci.* **62**, 2241–2257 (2017).
82. Figliuolo, V. R. et al. Sulfate-reducing bacteria stimulate gut immune responses and contribute to inflammation in experimental colitis. *Life Sci.* **189**, 29–38 (2017).
83. Kushkevych, I. et al. The sulfate-reducing microbial communities and meta-analysis of their occurrence during diseases of small–large intestine axis. *J. Clin. Med.* **8**, 1656 (2019).
84. Lin, L., Du, Y., Song, J., Wang, W. & Yang, C. Imaging commensal microbiota and pathogenic bacteria in the gut. *Acc. Chem. Res.* **54**, 2076–2087 (2021).
85. Ağagündüz, D. et al. Understanding the role of the gut microbiome in gastrointestinal cancer: A review. *Front. Pharmacol.* **14**, 1130562 (2023).
86. Dorman, C. J. Chapter 17 - Gene regulatory networks and hierarchies in bacterial pathogens. in *Molecular Medical Microbiology (Third Edition)* (eds. Tang, Y.-W. et al.) 337–355 https://doi.org/10.1016/B978-0-12-818619-0.00108-8 (Academic Press, 2024).
87. Lin, Q. et al. A review of the mechanisms of bacterial colonization of the mammal gut. *Microorganisms* **12**, 1026 (2024).
88. Shepherd, E. S., DeLoache, W. C., Pruss, K. M., Whitaker, W. R. & Sonnenburg, J. L. An exclusive metabolic niche enables strain engraftment in the gut microbiota. *Nature* **557**, 434–438 (2018).
89. Tomkovich, S. et al. An osmotic laxative renders mice susceptible to prolonged Clostridioides difficile colonization and hinders clearance. *mSphere* **6**, e0062921 (2021).
90. Clayton, C. A. et al. In mouse and gut-on-a-chip models, precolonoscopy bowel preparation promotes pathogen colonization of the gut and translocation to other organs. Preprint at https://doi.org/10.1101/2024.11.26.625504 (2024).
91. Maresca, D. et al. Nonlinear ultrasound imaging of nanoscale acoustic biomolecules. *Appl. Phys. Lett.* **110**, 073704 (2017).
92. Antoniou, E. et al. The TNBS-induced colitis animal model: An overview. *Ann. Med. Surg.* **11**, 9–15 (2016).
93. Roh, Y. Ultrasonic transducers for medical volumetric imaging. *Jpn. J. Appl. Phys.* **53**, 07KA01 (2014).

94. Jensen, J. A. et al. Anatomic and functional imaging using row–column arrays. *IEEE Trans. Ultrason. Ferroelectr. Freq. Control* **69**, 2722–2738 (2022).
95. Heiles, B. et al. Nonlinear sound-sheet microscopy: Imaging opaque organs at the capillary and cellular scale. *Science* **388**, eads1325 (2025).
96. Lee, S., Wu, D., Malounda, D., Rabut, C. & Shapiro, M. G. Real-time volumetric imaging of cells and molecules in deep tissues with Takoyaki ultrasound. Preprint at https://doi.org/10.1101/2024.11.14.623368 (2024).
97. Wang, C. et al. Bioadhesive ultrasound for long-term continuous imaging of diverse organs. *Science* **377**, 517–523 (2022).
98. La, T.-G. & Le, L. H. Flexible and wearable ultrasound device for medical applications: a review on materials, structural designs, and current challenges. *Adv. Mater. Technol.* **7**, 2100798 (2022).
99. Vega Preclinical Ultrasound System | Revvity. https://www.revvity.com/product/vega-preclinical-ultrasound-imaging-d5240000.
100. Mor-Avi, V. et al. Real-time artificial intelligence–based guidance of Echocardiographic imaging by novices: image quality and suitability for diagnostic interpretation and quantitative analysis. *Circ. Cardiovasc. Imaging* **16**, e015569 (2023).
101. Tenajas, R. et al. Recent advances in Artificial intelligence-assisted ultrasound scanning. *Appl. Sci.* **13**, 3693 (2023).
102. Namsena, P. et al. Diagnostic performance of artificial intelligence in interpreting thyroid nodules on ultrasound images: a multicenter retrospective study. *Quant. Imaging Med. Surg.* **14**, 3676–3694 (2024).
103. Shen, Y. et al. Artificial intelligence system reduces false-positive findings in the interpretation of breast ultrasound exams. *Nat. Commun.* **12**, 5645 (2021).
104. Freeling, J. L. & Rezvani, K. Assessment of murine colorectal cancer by micro-ultrasound using three dimensional reconstruction and non-linear contrast imaging. *Mol. Ther. Methods Clin. Dev.* **5**, 16070 (2016).
105. El Kaffas, A. et al. Molecular contrast-enhanced ultrasound imaging of radiation-induced p-selectin expression in healthy mice colon. *Int. J. Radiat. Oncol.* **97**, 581–585 (2017).
106. Sofroniew, N. et al. napari: a multi-dimensional image viewer for Python. *Zenodo* https://doi.org/10.5281/zenodo.7276432 (2022).
107. Herigstad, B., Hamilton, M. & Heersink, J. How to optimize the drop plate method for enumerating bacteria. *J. Microbiol. Methods* https://doi.org/10.1016/S0167-7012(00)00241-4 (2001).
108. Teague, B. Cytoflow: A Python Toolbox for Flow Cytometry. Preprint at https://doi.org/10.1101/2022.07.22.501078 (2022).
109. Bryan, J. T. & Daughenbaugh, P. J. Stabilized streptomycin solutions. (1955).
110. Nolte, T. et al. Nonproliferative and proliferative lesions of the gastrointestinal tract, pancreas and salivary glands of the rat and mouse. *J. Toxicol. Pathol.* **29**, 1S–125S (2016).
111. Abramson, J. et al. Accurate structure prediction of biomolecular interactions with AlphaFold 3. *Nature* 1–3 https://doi.org/10.1038/s41586-024-07487-w (2024).
112. Pettersen, E. F. et al. UCSF ChimeraX: Structure visualization for researchers, educators, and developers. *Protein Sci. Publ. Protein Soc.* **30**, 70–82 (2021).
113. Buss, M. shapiro-lab/Probiotic-GI-Imaging: Probiotic-GI-Imaging. Zenodo https://doi.org/10.5281/zenodo.15703247 (2025).

Acknowledgements

The authors thank the Caltech Flow Cytometry & Cell Sorting Facility for assistance with flow cytometry, Dr. Nathan Dalleska & the Water and Environment Lab (WEL) at Caltech for assistance with IC-MS, and Dr. Genevieve Remmers & IDEXX Laboratories for assistance with histopathology sample preparation and interpretation. The authors would also like to thank Dr. Moshe Baruch for assistance with sending the initial thiosulfate and tetrathionate sensor plasmids. MTB was supported by an NSF GRFP fellowship. This research was supported by the Pew Charitable Trust, the Institute for Collaborative Biotechnologies (US Army, W911NF-19-D-0001 to MGS), and the National Institutes of Health (NIAID R01AI155586 to JJT). Related research in the Shapiro Laboratory is supported by the David and Lucille Packard Foundation and the Dreyfus Foundation. MGS is an investigator of the Howard Hughes Medical Institute.

Author contributions

M.T.B. and M.G.S. conceived the study. M.T.B., L.Z., and J.H.K. planned and performed experiments. M.T.B. analyzed data. J.J.T. provided reagents and input on the research design and manuscript. M.T.B. and M.G.S. wrote the manuscript with input from all other authors. M.G.S. supervised the research.

Competing interests

The authors declare no competing interests.

Additional information

Supplementary information The online version contains supplementary material available at https://doi.org/10.1038/s41467-025-62569-1.

Correspondence and requests for materials should be addressed to Mikhail G. Shapiro.

Peer review information *Nature Communications* thanks the anonymous reviewers for their contribution to the peer review of this work. A peer review file is available.